The SAMI galaxy survey: galaxy size can explain the offset between star-forming and passive galaxies in the mass-metallicity relationship

Sam P. Vaughan[1,2]⋆, Tania M. Barone[1,2,3,4], Scott M. Croom[1,2], Luca Cortese[2,5], Francesco D'Eugenio[6,7], Sarah Brough[2,8], Matthew Colless[2,4], Richard M. McDermid[2,9], Jesse van de Sande[1,2], Nicholas Scott[1,2], Joss Bland-Hawthorn[1,2], Julia J. Bryant[1,2], J.S. Lawrence[12], Ángel R. López-Sánchez[2,9,11], Nuria P. F. Lorente[13], Matt S. Owers[2,9,10] and Samuel N. Richards[1]

[1]*Sydney Institute for Astronomy, School of Physics, Building A28, The University of Sydney, NSW 2006, Australia*
[2]*ARC Centre of Excellence for All Sky Astrophysics in 3 Dimensions (ASTRO3D), Australia*
[3]*Centre for Astrophysics and Supercomputing, School of Science, Swinburne University of Technology, Hawthorn, VIC 3122, Australia.*
[4]*Research School of Astronomy and Astrophysics, Australian National University, Canberra, ACT 2611, Australia*
[5]*International Centre for Radio Astronomy Research, The University of Western Australia, 35 Stirling Hw, 6009 Crawley, Australia*
[6]*Cavendish Laboratory and Kavli Institute for Cosmology, University of Cambridge, Madingley Rise, Cambridge, CB3 0HA, United Kingdom*
[7]*Sterrenkundig Observatorium, Universiteit Gent, Krijgslaan 281 S9, B-9000 Gent, Belgium*
[8]*School of Physics, University of New South Wales, NSW 2052, Australia*
[9]*Department of Physics and Astronomy, Macquarie University, NSW 2109, Australia*
[10]*Astronomy, Astrophysics and Astrophotonics Research Centre, Macquarie University, Sydney, NSW 2109, Australia*
[11]*Australian Astronomical Optics, Macquarie University, 105 Delhi Rd, North Ryde, NSW 2113, Australia*
[12]*Australian Astronomical Optics - Macquarie, Macquarie University, NSW 2109, Australia*
[13]*AAO-MQ, Faculty of Science & Engineering, Macquarie University, 105 Delhi Rd, North Ryde, NSW 2113, Australia*

ABSTRACT

In this work, we investigate how the central stellar metallicity ([Z/H]) of 1363 galaxies from the SAMI galaxy survey is related to their stellar mass and a proxy for the gravitational potential, $\Phi = \log_{10}\left(\frac{M_*}{M_\odot}\right) - \log_{10}\left(\frac{r_e}{\mathrm{kpc}}\right)$. In agreement with previous studies, we find that passive and star-forming galaxies occupy different areas of the [Z/H]-M_* plane, with passive galaxies having higher [Z/H] than star-forming galaxies at fixed mass (a difference of 0.23 dex at $\log_{10}(M_*/M_\odot)=10.3$). We show for the first time that all galaxies lie on the same relation between [Z/H] and Φ, and show that the offset in [Z/H] between passive and star-forming galaxies at fixed Φ is smaller than or equal to the offset in [Z/H] at fixed mass (an average Δ[Z/H] of 0.11 dex at fixed Φ compared to 0.21 dex at fixed mass). We then build a simple model of galaxy evolution to explain and understand our results. By assuming that [Z/H] traces Φ over cosmic time and that the probability that a galaxy quenches depends on both its mass and size, we are able to reproduce these offsets in stellar metallicity with a model containing instantaneous quenching. We therefore conclude that an offset in metallicity at fixed mass cannot by itself be used as evidence of slow quenching processes, in contrast to previous studies. Instead, our model implies that metal-rich galaxies have always been the smallest objects for their mass in a population. Our findings reiterate the need to consider galaxy size when studying stellar populations.

Key words: galaxies: abundances – galaxies: evolution – galaxies: formation

1 INTRODUCTION

Galaxies in the Universe can broadly be classified into two categories: those which are currently forming stars and those which are not. Understanding and quantifying exactly which physical processes play a role in shaping this dichotomy is a fundamental goal of galaxy evolution, but despite decades of work on the topic (e.g. Tinsley 1968; Larson et al. 1980; Dekel & Birnboim 2006; Peng et al. 2010; Schawinski et al. 2014, among many others) a complete picture remains out of reach.

In the most popular framework for discussing the life cycles of galaxies, the idea of star formation "quenching" plays a central role. This model envisions that the natural state of a galaxy is to be forming stars at a rate which places it on the "main-sequence" of star-formation (Noeske et al. 2007; Speagle et al. 2014; Renzini & Peng 2015). Internal or external processes then act to stop the galaxy's star formation, causing it to transition off the main sequence and join the passive population. The question of "what leads to the division in galaxy properties?" can then be reframed as "what causes quenching?". A wide range of physical drivers of quenching have been proposed and investigated, including feedback from a galaxy's central black hole (Silk & Rees 1998; Magorrian et al. 1998; Di Mat-

⋆ Contact e-mail: sam.vaughan@sydney.edu.au (SPV)

teo et al. 2005), the effects of falling into a massive galaxy cluster (Gunn & Gott 1972; Abadi et al. 1999), the secular evolution of stellar orbits over cosmic time (Kormendy & Kennicutt 2004; Sellwood 2014) and the occurrence of "compaction" events which increase a galaxy's central surface density (e.g. Woo et al. 2015; Woo & Ellison 2019).

Finding direct evidence of quenching in an individual object by catching such processes in the act is notoriously difficult, however, since we lack the ability to study individual galaxies across cosmic time. The few examples we do have tend to be of extremely rapid quenching via the removal of a galaxy's supply of cold gas, such as in the case of "Jellyfish" galaxies falling into massive cluster potentials (e.g. Gunn & Gott 1972; Smith et al. 2010; numerous observations from the "GAs Stripping Phenomena in galaxies with MUSE" survey of Poggianti et al. 2017). Whilst spectacular, these examples are clearly not typical of the type of quenching which the majority of galaxies in the Universe undergo.

Another route to approach the problem is by studying a large sample of galaxies and investigating the properties of the entire population as a whole. This was the approach taken by Peng et al. (2015, hereafter P15) and Trussler et al. (2020, hereafter T20), who used the stellar ages and metallicities of tens of thousands of galaxies from the Sloan Digital Sky Survey (SDSS; York et al. 2000; Eisenstein et al. 2011; Blanton et al. 2017) in the nearby Universe to conclude that quenching processes must be slow in nature, with quenching timescales of the order of 4 Gyrs.

Key to their conclusions is the correlation between stellar mass and stellar metallicity, and the fact that quiescent galaxies tend to be more metal rich than star forming galaxies at fixed mass (P15; T20). Previous studies have discussed that the size of a galaxy is also an important parameter to consider when analysing its stellar populations (e.g. McDermid et al. 2015; Scott et al. 2017). Furthermore, recent work by Barone et al. (2018), D'Eugenio et al. (2018) and Barone et al. (2020) has quantified this fact: they find that the metallicity of gas and stars in galaxies forms a tighter relationship with a combination of mass and size ($\Phi = \log_{10}\left(\frac{M_*}{M_\odot}\right) - \log_{10}\left(\frac{r_e}{\mathrm{kpc}}\right)$, a proxy for the galaxy's gravitational potential) compared to the relationship between metallicity and stellar mass alone.

Given that, at fixed stellar mass, star-forming galaxies are larger than passive galaxies (Shen et al. 2003; Lange et al. 2015), they also have shallower gravitational potentials. Taken together, these results beg the question of whether the difference in metallicity between passive and star-forming galaxies at fixed stellar mass discussed by P15 and T20 is still evident at fixed Φ. Can quenching processes which depend on both mass *and size* be used to explain the diversity of galaxies we observe today in the local Universe?

In this work, we build on the previous studies of Barone et al. (2018, 2020) and D'Eugenio et al. (2018) and, for the first time, investigate the correlations between stellar metallicity, stellar mass and gravitational potential for a homogeneously-observed sample containing both quiescent and star-forming galaxies together, instead of studying each class of galaxy separately. We then ask a similar question to P15 and T20: what can we learn about the quenching timescales of galaxies from these observations? One key difference between our sample and that of P15 and T20 is that each galaxy we study has a robust half-light radius measurement, allowing us to investigate the roles of mass and size in regulating galaxy quenching processes and the production of metals. We also have the advantage of using spatially resolved observations instead of the fixed apertures used by P15 and T20. This means that we can limit the common issue

of aperture bias resulting from probing galaxies of different apparent sizes (and radial gradients in metallicity) to varying degrees.

The outline of this paper is as follows. In Section 2 we briefly introduce the SAMI galaxy survey and describe the stellar mass and half-light radius measurements we will be using. In Section 3 we describe our sample of galaxies and outline our method to measure stellar metallicities. Section 4 describes our techniques for fitting straight lines to our measurements to infer metallicity gradients and central values. In Section 5 we present our results and in Section 6 we discuss our findings, introducing a simple toy model of galaxy quenching to reproduce the population of local galaxies in Section 6.2. In Section 7 we draw our conclusions. We assume a flat Λ cold dark matter (ΛCDM) cosmology with $\Omega_\Lambda = 0.7$, $\Omega_M = 0.3$, and $H_0 = 70\,\mathrm{kms}^{-1}\mathrm{Mpc}^{-1}$. We also assume a Chabrier (2003) initial mass function where necessary.

2 THE SAMI SURVEY AND ANCILLARY DATA

The galaxies in this work are drawn from data release 3 (DR3) of the SAMI galaxy survey (Croom et al. 2021a). SAMI DR3 provides fully reduced datacubes for 3068 galaxies in the local Universe, selected to have a redshift (z) less than 0.11 and a stellar mass between $7.8 \leq \log_{10}(M_*/M_\odot) \leq 11.8$. The SAMI instrument (Croom et al. 2012) is mounted at the prime focus on the Anglo-Australian Telescope that provides a 1 degree diameter field of view. SAMI uses 13 fused fibre bundles ("Hexabundles"; Bland-Hawthorn et al. 2011; Bryant et al. 2014) with a high (75%) fill factor. Each bundle contains 61 fibres of 1.6″ diameter resulting in each IFU having a diameter of 15″. The IFUs, as well as 26 sky fibres, are plugged into pre-drilled plates using magnetic connectors. SAMI fibres are fed to the double-beam AAOmega spectrograph (Sharp et al. 2006). AAOmega allows a range of different resolutions and wavelength ranges. The SAMI Galaxy survey uses the 570V grating at 3700-5700Å giving a resolution of $R = 1730$ ($\sigma = 70.4$ km s^{-1}), and the R1000 grating from 6250-7350Å giving a resolution of $R = 4500$ ($\sigma = 29.6$ km s^{-1}).

For each galaxy, we also require a number of ancillary measurements for our analysis. Stellar masses for each SAMI galaxy were derived using $g - i$ colours and the prescription of Taylor et al. (2011), updated in Bryant et al. (2015). Total star formation rates (SFRs) were derived from Hα flux measurements by Medling et al. (2018), with an aperture correction applied where appropriate. As discussed in Medling et al. (2018), these SFR measurements should be considered as lower limits, since spaxels with contribution to the Hα flux from shocks or AGN are removed before a global SFR is calculated. Furthermore, low surface brightness Hα emission may be below the detection limits adopted. This will tend to bias low-mass galaxies to lower SFRs. We therefore choose to use the relation between SFR and stellar mass from Renzini & Peng (2015) to classify galaxies as star-forming, intermediate or quiescent, rather than fitting to the SAMI SFR and mass measurements ourselves (see Section 3).

Half-light radii were measured using the Multi-Gaussian expansion method of Cappellari (2002) from r-band images of each object (D'Eugenio et al. 2021). The photometry is drawn from the Sloan Digital Sky Survey data release 7 (Abazajian et al. 2009) and 9 (Ahn et al. 2012), as well as the VLT Survey Telescope's ATLAS Survey (Shanks et al. 2015). See D'Eugenio et al. (2021) for further details.
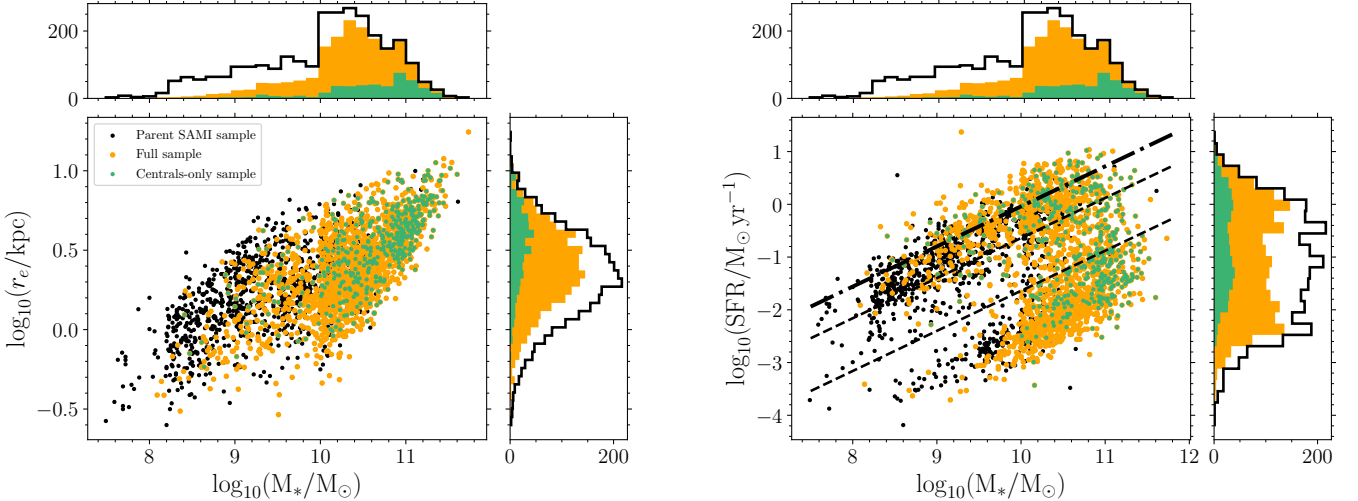
Figure 1. The mass-size plane (left) and mass-SFR plane(right) of our sample. Each panel shows the parent SAMI catalogue (black), the galaxies which form our "full" sample (orange) and those which are part of the "centrals-only" sample (green), as discussed in Section 3. Histograms show the distribution of each parameter. In the mass-SFR plane, we also show the star forming sequence from Renzini & Peng (2015), which we use to classify galaxies as star-forming, passive or intermediate: star-forming galaxies are above the highest dashed line; quenched galaxies are below the lower dashed line; intermediate galaxies are between the dashed lines.

3 STELLAR POPULATION MEASUREMENTS AND SAMPLE SELECTION

We measure stellar population parameters as a function of radius for each galaxy in the sample. A full description of these measurements used in this work will be presented in a forthcoming paper (Vaughan et al. in prep). We give a brief summary here. Firstly, the blue and red arm spectra are joined together and convolved with a Gaussian kernel (of variable width) such that the spectral resolution is a constant value at all wavelengths (followong van de Sande et al. 2017). We then use the Voronoi binning algorithm of Cappellari & Copin (2003) to aggregate spectra together such that their combined spectrum has a minimum signal-to-noise (S/N) ratio of 20 Å^{-1} in the V-band. Individual spaxels with a S/N above 20 Å^{-1} are left unbinned. 181 galaxies lacked the required S/N to create a single Voronoi bin and were discarded. At this stage, we remove from our sample any galaxies which have fewer than 10 independent Voronoi bins or have $\log_{10}(M_*/M_\odot) < 8$. We also remove interacting galaxies or galaxies with close companions. This leaves us with 78,531 spectra from 1363 galaxies, which we call the "full sample".

We then use the penalised-pixel fitting code pPXF (Cappellari & Emsellem 2004; Cappellari 2017) to fit the MILES simple stellar population (SSP) models of Vazdekis et al. (2015) to the spectrum from each Voronoi bin. The templates range in metallicity from -2.21 dex to 0.4 dex, in age from 30 Myrs to 14 Gyrs and in [α/Fe] abundance from 0.0 to +0.4 dex. The templates use the isochrones from the "Bag of Stellar Tracks and Isochrones" models (BaSTI; Pietrinferni et al. 2004, 2006).

In Appendix B, we investigate the use of the Binary Population and Spectral Synthesis models (BPASS: Eldridge et al. 2017; Stanway & Eldridge 2018; Byrne et al. 2022) as an alternative to the MILES SSPs. We find the stellar metallicity values derived using BPASS are offset to lower values of [Z/H], and there is also a difference in the derived slopes of the correlations between stellar metallicity and mass and stellar metallicity and Φ. However, our overall conclusions from Section 5 remain unchanged. See Appendix B for further details.

In essence, pPXF finds the weighted sum of SSP templates which best recovers the input galaxy spectrum. We also include gas emission line templates corresponding to the Balmer series (Hα, Hβ and Hγ) as well as the atomic species [N II], [O III], [S II], and [O I]. We use a multiplicative Legendre polynomial of order 10 to correct for small differences in the shape of the observed and template spectra. We normalise the SSP spectra such that the resulting stellar population parameters are mass-weighted. We also measured the stellar population parameters from the spectra extracted from within the half-light radius (r_e) of each galaxy in the same manner, and find that our conclusions remain unchanged.

We estimate the uncertainties on our mass-weighted metallicity measurements by selecting a sample of 10,000 spectra and bootstrapping their measurements 50 times. We then build a simple model to predict this bootstrapped uncertainty ($\sigma_{[Z/H]}$) from the spectrum's [Z/H] and signal-to-noise ratio. This model is then applied to the remaining spectra. Further details of our uncertainty modelling are given in Appendix A.

Finally, we also create a "central-only sample" to differentiate between galaxies which are dominant in their dark matter halos ("centrals") and those which are not ("satellites"). We use the Galaxy and Mass Assembly (GAMA) galaxy group catalogue (G^{3}C) of Robotham et al. (2011). In practice, the G^{3}C catalogue selects objects which are the brightest galaxy in the r-band within each group to be "centrals". It should be noted that these galaxies are not guaranteed to be the most massive in their group. We include isolated galaxies as centrals. The goal of the central-only sample is to create a sample of objects which have primarily undergone (or will undergo) *internal* quenching processes (in contrast to quenching processes which depend on environment, which predominantly influence satellite galaxies: see e.g. Woo et al. 2017). We will use this sample to compare to the quenching toy model presented in 6.2, since the model does not include any prescription for environmental quenching. Our central-only sample contains 527 galaxies, 39% of the full sample.

Plots of the mass-size and mass-SFR planes for the SAMI parent catalogue and our samples are shown in Figure 1. We classify galaxies
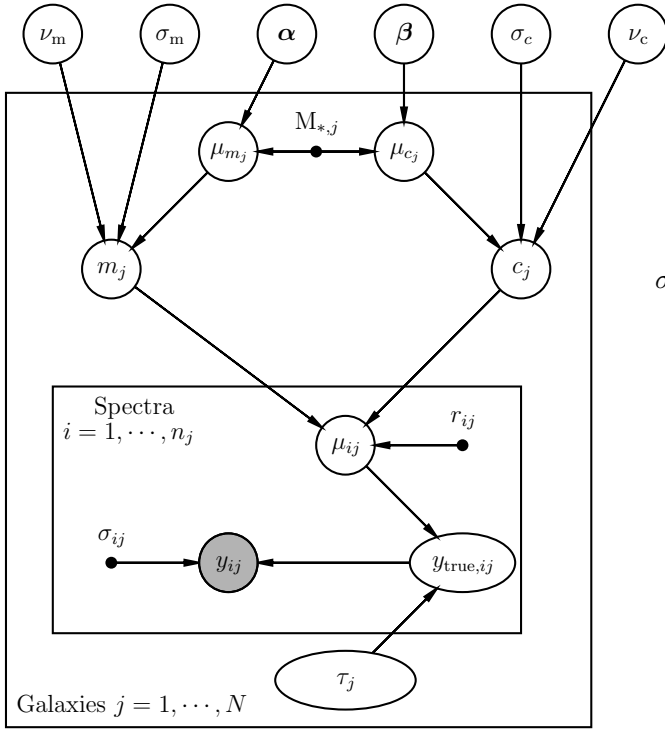
Figure 2. A graphical representation of our hierarchical model (left) and a mathematical description of the priors and hyperpriors used (right). See Section 4.2 for a full discussion.

$$\boldsymbol{\alpha} \sim \mathcal{N}(0,0.3), \quad \boldsymbol{\beta} \sim \mathcal{N}(0,0.1) \tag{1}$$

$$\nu_m \sim \mathrm{Gamma}(2,0.1), \quad \nu_c \sim \mathrm{Gamma}(2,0.1) \tag{2}$$

$$\sigma_m \sim \mathcal{N}^+(0,1), \quad \sigma_c \sim \mathcal{N}^+(0,1), \quad \tau_j \sim \mathcal{N}^+(0,1) \tag{3}$$

$$\mu_{m_j} = \alpha_0 + \alpha_1 \mathrm{M}_{*,j} \tag{4}$$

$$\mu_{c_j} = \beta_0 + \beta_1 \mathrm{M}_{*,j} \tag{5}$$

$$m_j \sim \mathrm{Student-T}(\nu_m, \mu_{m_j}, \sigma_m) \tag{6}$$

$$c_j \sim \mathrm{Student-T}(\nu_c, \mu_{c_j}, \sigma_c) \tag{7}$$

$$\mu_{ij} = m_j r_{ij} + c_j \tag{8}$$

$$y_{\mathrm{true},ij} \sim \mathcal{N}(\mu_{ij}, \tau_j) \tag{9}$$

$$y_{ij} \sim \mathcal{N}(y_{\mathrm{true},ij}, \sigma_{ij}) \tag{10}$$

as being star-forming or passive using simple cuts in the mass-SFR plane. Following Renzini & Peng (2015), we define the star-forming "main sequence" to be

$$\log(\mathrm{SFR}) = 0.76 \log(\mathrm{M}_*/\mathrm{M}_\odot) - 7.64 \tag{1}$$

with a scatter around the relation of 0.3 dex. We define the difference between a galaxy's measured star-formation rate (SFR) and the SFR of a galaxy of the same mass on the main sequence as $\Delta\mathrm{SFR_{MS}}$. Following other papers in the literature (e.g. Croom et al. 2021b), we separate galaxies into star-forming, intermediate (or "green-valley") or passive in the following manner:

$$\mathrm{SF\ galaxies} : \Delta\mathrm{SFR_{MS}} > -0.6 \tag{2}$$

$$\mathrm{Green-valley\ galaxies} : -0.6 \leq \Delta\mathrm{SFR_{MS}} \leq -1.6 \tag{3}$$

$$\mathrm{Passive\ galaxies} : \Delta\mathrm{SFR_{MS}} < -1.6 \tag{4}$$

In essence, this definition requires star-forming galaxies to be within 2σ (0.6 dex) of the main sequence; passive galaxies to be more than 5σ from the main sequence (1.6 dex); and intermediate galaxies to fall between these two categories. Reasonable changes to these values have no effect on our conclusions. Our full sample consists of 442 star-forming galaxies, 694 passive galaxies and 227 intermediate galaxies.

4 MEASURING METALLICITY GRADIENTS AND INTERCEPTS

For every galaxy in the full sample, we infer the stellar metallicity at the very centre of the galaxy (galacto-centric radius $r = 0$) by fitting

a straight line to the metallicity measurements as a function of radius. We perform this fit in two different ways, with our conclusions the same in each case. A reader uninterested in the technical details of the fitting can safely skip this section and move on to the results in Section 5. We note that our conclusions are also unchanged if we instead use the stellar metallicities found from the $1r_e$ spectra instead of the central metallicity of each galaxy, as shown in Appendix C.

4.1 Simple straight line fits

First, we perform a simple straight-line fit to the [Z/H] measurements in each galaxy as a function of r/r_e, where r_e is the half-light radius of the galaxy. For reasons which will become clear shortly, we refer to this as the "unpooled" fit.

For each galaxy j we measure a metallicity gradient, m_j, metallicity at $r = 0$, c_j, and the intrinsic scatter around the best-fit straight line, τ_j. If each galaxy has n_j metallicity measurements, y_{ij}, at radius r_{ij} with uncertainty σ_{ij}, our likelihood function for each galaxy takes the form

$$\log \mathcal{L}_j \propto \sum_{i=0}^{i=n_j} \left(\frac{(y_{ij} - (m_j r_{ij} + c_j))^2}{\sigma_{ij}^2 + \tau_j^2} \right) \tag{5}$$

To perform the fit, we apply weakly informative Gaussian priors of $\mathcal{N}(0,1)$ to each m_j and c_j, and weakly informative half-Gaussian priors of $\mathcal{N}^+(0,1)$ to each τ_j (to ensure the τ_j always remain positive).[1]

---

[1] $\mathcal{N}(\mu, \sigma)$ refers to a Gaussian distribution of mean μ and standard deviation σ. $\mathcal{N}^+(\mu, \sigma)$ is a "half-Gaussian" function which is constrained to only be non-zero for positive values of the dependent variable.

We perform the fit using the probabilistic programming language STAN (Carpenter et al. 2017) and its python interface PYSTAN[2], which performs full Bayesian inference of the posterior distribution using an implementation of the No U Turn sampler (NUTS; Hoffman & Gelman 2014). We performed 1000 warm-up transitions and 1000 draws from the posterior using 4 independent chains. We ensured that there were no divergent transitions and that the potential scale reduction factor $\hat{R}$ (Gelman & Rubin 1992) was always within acceptable limits (between 1 and 1.1). We take the best fitting value of each parameter to be its posterior mean and its uncertainty to be the standard deviation of the posterior samples.

Our unpooled fit suffers from two issues. Firstly, galaxies with few metallicity measurements will have large uncertainties on their derived parameters. Secondly, the highest and lowest metallicity templates used in this work are +0.4 dex and -2.21 dex, and 695 and 78 spectra hit these upper and lower limits respectively. The correct way to treat these measurements is as "right censored" or "left censored" data, since we only know that their true metallicity value is *at least* 0.4 dex or *at most* -2.2 dex.

We now build a model to address each of these issues.

4.2 More complicated fits: hierarchical modelling and censored data

We also measure m_j, c_j and τ_j for each galaxy using a hierarchical Bayesian model. The idea of a hierarchical model is to share or "pool" information between "groups" within a set of data, in order to obtain tighter constrains than in the unpooled case above. Here, our metallicity measurements are naturally grouped by the galaxy they are observed from. For galaxies with few metallicity measurements, where the unpooled model may return more uncertain results, a hierarchical model can "share" constraints from similar galaxies to get the tightest inferences on m and c.

Another way to think about the hierarchical model is in terms of the priors we apply to each galaxy. In the unpooled model, these priors are identical and fixed for each object. In a hierarchical model, we use hyperparameters to modify the priors for each galaxy depending on other quantities of interest (in this case, stellar mass). This allows us to place different priors on the central metallicity a galaxy of $10^{11} M_\odot$ compared to a galaxy of $10^8 M_\odot$ (for example). The key point is that we do not put these different priors in by hand; *they are also estimated from the data during the fitting process*. An introduction to hierarchical models can be found in Gelman et al. (2013), and some examples of their use in astronomy can be found in Lieu et al. (2017); Varidel et al. (2020); Grumitt et al. (2020) and Vaughan et al. (2020).

Figure 2 shows a graphical representation of our hierarchical model. We place a Student's T distribution[3] prior on the gradients, m_j, and intercepts, c_j (Figure 2, lines 6 and 7). The central location of these priors, μ_{mj} and μ_{cj}, vary linearly with stellar mass (Figure 2 lines 4 and 5) with coefficients $\boldsymbol{\alpha} = (\alpha_0, \alpha_1)$ and $\boldsymbol{\beta} = (\beta_0, \beta_1)$ respectively. These priors incorporate the information that metallicity, metallicity gradients and galaxy stellar mass are correlated and can be described by linear relations (e.g. Gallazzi et al. 2005, P15; T20, Goddard et al. 2017; Zheng et al. 2017; Li et al. 2018; Santucci

---

[2] https://pystan.readthedocs.io/en/latest/index.html
[3] A Student's T distribution is described by three parameters; a location (μ), a scale (σ) and a "degree of freedom" or "normality" parameter (ν). As ν becomes large, the Student's T probability distribution tends towards a Gaussian.

Table 1. Results from the straight line fits to the mass-metallicity relation for star-forming, passive and intermediate ("green valley") galaxies. We fit relations of the form $[Z/H] = m(\log_{10}(M_*/M_\odot) - 10.3) + c$. The difference in metallicity between galaxies at a fixed mass of $10^{10.3}$ $M_\odot$ is in very good agreement with Peng et al. (2015) and Trussler et al. (2020).

	m	c
Star-forming	0.72 ± 0.02	-0.07 ± 0.01
Intermediate	0.57 ± 0.02	-0.00 ± 0.01
Passive	0.26 ± 0.01	0.16 ± 0.00

et al. 2020). The remaining hyperparameters are given fixed priors as described in Figure 2 (lines 1 through 3).

For the spectra with metallicity values at the limits of our templates, we modify the likelihood function to treat these observations as "censored" data. Using our Gaussian likelihood function, the probability that a measurement has a value greater than a value U is given by

$$\Pr[y > U] = \int_U^\infty \mathcal{N}(y|\mu, \sigma)dy = 1 - \Phi\left(\frac{y - \mu}{\sigma}\right)$$

where Φ is the standard normal cumulative distribution function. We can therefore simply sum each censored contribution to the log likelihood function as

$$\log \mathcal{L}_{\text{right censored}} = \sum_{i,j}\left(1 - \Phi\left(\frac{y_{ij} - \mu_j}{\sigma_j}\right)\right)$$

and add this contribution to the likelihood function for the uncensored data. Similarly, for data less than a value L

$$\Pr[y < L] = \int_{-\infty}^L \mathcal{N}(y|\mu, \sigma)dy = \Phi\left(\frac{y - \mu}{\sigma}\right)$$

and

$$\log \mathcal{L}_{\text{left censored}} = \sum_{i,j} \Phi\left(\frac{y_{ij} - \mu_j}{\sigma_j}\right)$$

We again use STAN to perform perform the fitting, again performing 1000 warm up transitions and 1000 draws from the posterior for 4 independent chains. We take the best fitting value of each parameter to be its posterior mean and the standard deviation of the posterior samples to be the uncertainty.

The results in this paper all use the hierarchical model, although we find that our conclusions are unchanged if we instead use the simple unpooled results. A quantitative comparison of the two is presented in Appendix E.

5 RESULTS

The main result of this work is the relationship between the central metallicity of galaxies ($[Z/H]_0$, as measured from their radial metallicity gradients) and a proxy for their gravitational potential, $\Phi = \log_{10}\left(\frac{M_*}{M_\odot}\right) - \log_{10}\left(\frac{r_e}{\text{kpc}}\right)$. This is presented in Figure 3.

We show the results of our central metallicity measurements as a function of mass in the left hand panel of Figure 3, with SF galaxies coloured blue, passive galaxies shown in red and intermediate galaxies in yellow. Quantitative results of fitting a straight line to the star-forming and passive galaxies are shown in Table 1.

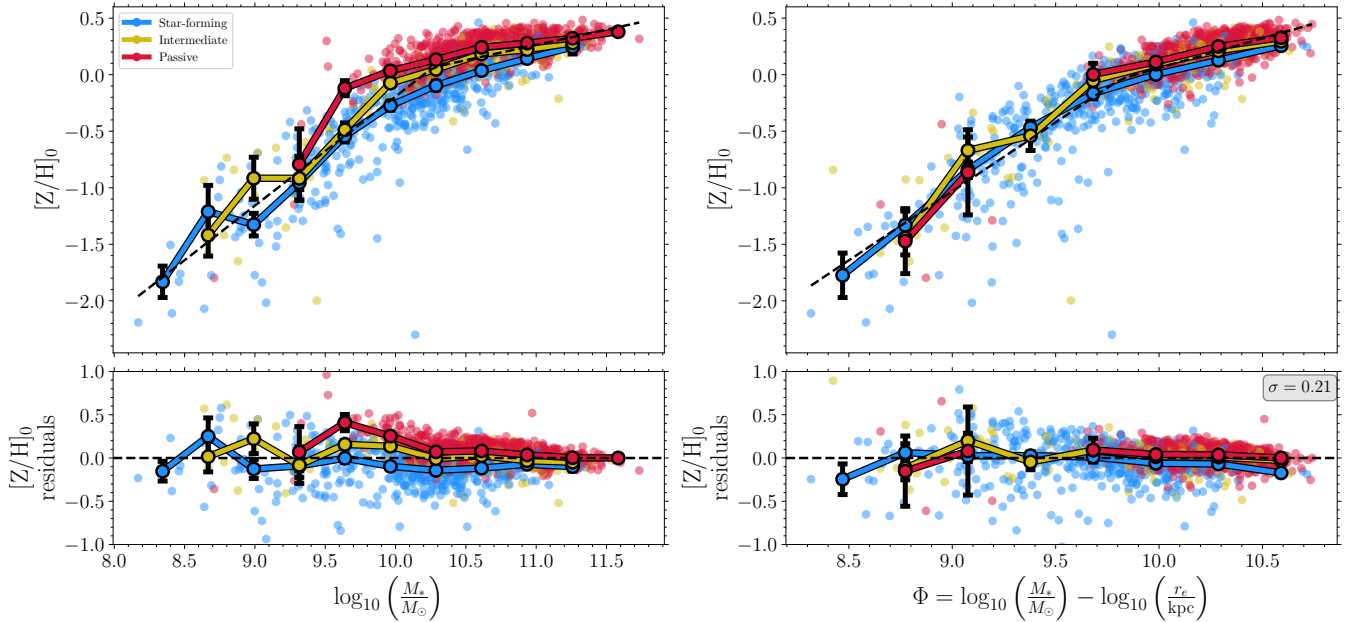We confirm the well known result that passive and SF galaxies

Figure 3. Mass-metallicity (left) and Φ-metallicity (right) relations for our SAMI galaxies. The metallicity measurements are mass-weighted and measured at the centre of each galaxy (see Section 3). We separate our sample into passive, star-forming and intermediate ("green valley") galaxies according to the definition in Renzini & Peng (2015). The large circles and coloured lines show the median value of $[Z/H]_0$ for star-forming, intermediate and passive galaxies in bins of width 0.3 dex. Black error bars show the standard error on the median. The dashed lines in each panel show a broken-line fit to all galaxies. The lower panels show the residuals around the dashed lines as a function of stellar mass (left) and gravitational potential (right). We measure the intrinsic scatter around the $[Z/H]_0$-Φ relation to be 0.21 dex. The offsets between passive, intermediate and star-forming galaxies in the mass-metallicity plane are in very good agreement to those measured in Trussler et al. (2020) and Peng et al. (2015). The right-hand panel shows that all galaxies form a much tighter sequence in the $[Z/H]_0$-Φ plane, showing that accounting for galaxy size reduces the difference between star-forming and passive galaxies.

occupy different areas of the mass-metallicity plane, and that passive galaxies tend to be more metal-rich than SF galaxies at the same mass. The straight line fits to the mass-metallicity relation are in excellent agreement with the recent work of P15 and T20; we find that, at a stellar mass of $\log(M_*/M_\odot) = 10.3$, the offset in metallicity between star-forming and passive galaxies is 0.23 dex, compared to 0.2–0.25 dex from T20. We also measure a difference in metallicity between star-forming and intermediate galaxies to be 0.07 dex at $\log(M_*/M_\odot) = 10.3$, very similar to the 0.06–0.012 dex measured in T20.

This difference in metallicity between star-forming and passive galaxies is mass dependent, dropping to a smaller value of 0.07 dex at the high-mass end of our sample, again in agreement with P15 and T20. This is shown in the left hand panel of Figure 4.

The right hand panel of Figure 3, shows the mass-weighted central metallicity of each galaxy against a proxy for its gravitational potential, Φ, where $\Phi = \log_{10}\left(\frac{M_*}{M_\odot}\right) - \log_{10}\left(\frac{r_e}{\text{kpc}}\right)$. This plot shows that the metallicity difference between the average star-forming and passive galaxy at fixed Φ, rather than fixed mass, is much smaller. As discussed in Barone et al. (2018, 2020), for both passive and star-forming galaxies, stellar metallicity correlates better with Φ than mass (as quantified by the intrinsic scatter around the relation). Here, we show for the first time that the distributions of star-forming and passive galaxies in the $[Z/H]$-Φ plane smoothly follow on from one another.

We also show the difference in metallicity at fixed Φ between star-forming, passive and intermediate galaxies in the right-hand panel of Figure 4. It is clear that the metallicity offset at fixed Φ between passive and star-forming galaxies is reduced compared to when using

mass: the largest difference is 0.14 dex at $\Phi = 9.5$, compared to a difference of 0.38 dex at $\log_{10}(M_*/M_\odot) = 9.6$, and the average offset across all bins in Φ is 0.11 dex, compared to the average across all bins in mass of 0.21 dex. It is only for the highest mass bin where the $\Delta[Z/H]$ values are comparable, being 0.08 dex for the rightmost points in each panel. The difference at fixed Φ is also approximately constant, being consistent with a single offset of 0.11 ± 0.03 dex at all values of Φ.

If we use the spectra extracted from $1r_e$ for each galaxy instead of the central values of $[Z/H]$ inferred from our hierarchical model, we find a very similar result: the average offset in $[Z/H]$ between passive and star-forming galaxies across all bins in Φ is 0.07 ± 0.03 dex.

We fit a broken line model to all galaxies in the Φ-$[Z/H]$ and mass-$[Z/H]$ planes, described by

$$[Z/H] = \begin{cases} c + m_u\Phi & \text{if } \Phi \geq \Phi_b \\ c + m_l\Phi + (m_u - m_l)\Phi & \text{if } \Phi < \Phi_b \end{cases} \quad (6)$$

This broken line has 5 free parameters: the breakpoint, Φ_b; the slope of the line below the break, m_l; the slope of the line above the break, m_u; an intercept, c; and the intrinsic scatter around the relation, σ. We show the best-fit broken line model for all galaxies as a dotted line in Figure 3.

We also highlight here how the right-hand panel of Figure 3 might change were we to use half-mass radii rather than half-light radii to calculate Φ, although a full analysis of this point is beyond the scope of this work. As discussed in Suess et al. (2019), the half-mass radii of low-redshift quiescent galaxies tend to be a fixed fraction of their half-light radii whereas the ratio of $r_{e,\text{mass}}/r_{e,\text{light}}$ for star-forming
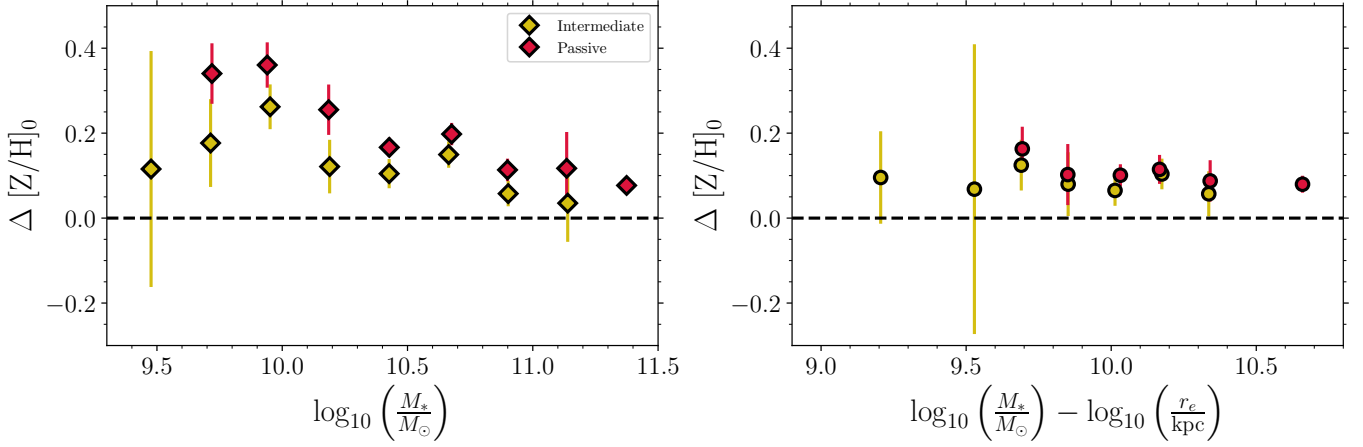
Figure 4. The difference in metallicity between star-forming and passive galaxies (red points) and star-forming and intermediate galaxies (yellow points) as a function of mass (left) and Φ (right). Each point represents the median metallicity difference of our sample in bins of mass (left) and Φ (right). We only show bins which contain at least 5 galaxies. Error bars represent the sum in quadrature of the standard error on the median of the star-forming bin and the passive/intermediate bin as appropriate.

galaxies decreases as their mass increases, becoming only ≈ 0.6 for galaxies with $\log_{10}(M_*/M_\odot) \approx 11$. This would tend to move high-mass star-forming galaxies to the right in Figure 3, increasing the scatter around the [Z/H]-Φ relation and accentuating its break.

6 DISCUSSION

Many previous studies have discussed the correlations between a galaxy's stellar metallicity and its structural parameters, although predominantly in terms of velocity dispersion σ (e.g. Trager et al. 2000; Thomas et al. 2005; Nelan et al. 2005; Graves et al. 2009a,b; McDermid et al. 2015; Scott et al. 2017; Li et al. 2018) rather than Φ as in this work.

The two quantities are obviously closely related; assuming galaxies are virialised, $\sigma^2 \propto M/R$. We show this relationship between central velocity dispersion, σ, and $\Phi = \log_{10}\left(\frac{M_*}{M_\odot}\right) - \log_{10}\left(\frac{r_e}{\text{kpc}}\right)$ for the full sample in Appendix D, which clearly shows the expected linear correlation with a gradient of 2 for galaxies with σ greater than the SAMI blue-arm instrumental resolution (of $\approx 70\,\text{kms}^{-1}$). We use Φ in this work to allow us to extend Figure 3 to the lowest values of Φ in our sample, without the complication of measuring velocity dispersion values close to (or below) the instrumental resolution. However, we note that there may be other, physical reasons why galaxies with low values of Φ depart from the simple linear relationship with σ: e.g. perhaps due to an excess of dark-matter, as proposed in Barat et al. (2019) and Barat et al. (2020).

Barone et al. (2018) and Barone et al. (2020) were the first to show quantitatively that stellar metallicities correlated tightly with the purely photometric quantity $\Phi \sim M/r_e$, and that this correlation was tighter than for stellar mass alone. Their work concentrated first on early-type galaxies and then on star-forming galaxies, however, without drawing conclusions about a combined sample. Here, we show for the first time that star-forming, intermediate and quiescent galaxies all lie on the same relation in the [Z/H]-Φ plane.

The physical mechanism which drives this relation is not yet fully understood, but is likely due to the relationship between mass, size and the local escape velocity of the system (e.g. Franx & Illingworth 1990; Emsellem et al. 1996; Scott et al. 2009, 2017). Galaxies with deeper potential wells are more able to retain the metal-rich winds and ejecta from massive stars which pollute their interstellar media, meaning that their future generations of stars will be more metal rich than those in galaxies with shallower potential wells. We note however, that this simple pictures complicates if the [Z/H]–Phi relation changes with redshift- a matter we discuss further in Section 6.3.

The fact that galaxies in our sample follow a single [Z/H]-Φ relation has interesting implications for large photometric surveys of galaxies. Section 5 shows that stellar metallicity can be determined solely from photometric observations of r_e and M_* to a 1-σ accuracy of ≈ 0.2 dex.

To date, estimating stellar metallicities without spectroscopic information, using broad-band colours or via panchromatic spectral energy distribution (SED) fitting, is notoriously unreliable. Many SED fitting codes therefore treat stellar metallicity as a nuisance parameter or fix it at solar metallicity (e.g. Skelton et al. 2014, and see the discussion in Conroy 2013). Other studies have shown that the choice of different stellar population synthesis models gives different results for the same input colours (Lee et al. 2007; Eminian et al. 2008; Conroy 2013). Stellar masses, on the other hand, are much more straightforward and robust outputs of SED fitting (due to the fortuitous degeneracies which exist between dust, age, and metallicity: Bell & de Jong 2001; Taylor et al. 2011; van de Sande et al. 2015).

Further work into the [Z/H]-Φ relation could therefore allow for the estimation of stellar metallicities for large catalogues of galaxies without expensive spectroscopic observations for the first time. Whilst the correlation in Figure 3 has till now only been investigated in the low-redshift Universe, calibrating this relationship at higher redshift could allow for studies of stellar metallicity over cosmic time (see also Barone et al. 2022, who find the [Z/H]-Φ relation of passive galaxies at z=0.7).

6.1 Implications for galaxy quenching

T20 and P15 use the difference in metallicity between star-forming and passive galaxies at $z = 0$ to conclude that most galaxies in the Universe undergo slow quenching ("starvation"). Their argument is as follows. During the course of stellar evolution, the stars in a

galaxy will convert hydrogen and helium into heavier elements. A fraction of the stars in a galaxy will return their metal content to the interstellar medium (through supernovae or mass-loss from stellar winds), which increases the galaxy's overall gas-phase metallicity. On the other hand, accretion of pristine gas from the galaxy's halo or cosmic filaments will tend to dilute a galaxy's gas reservoir and lower its metallicity. The balance of these two processes sets whether a galaxy's next generation of stars will tend to have a lower, higher or similar stellar metallicity to previous generations.

If a galaxy's supply of cold gas is quickly removed or star formation is quickly suppressed, both of these processes are stopped and the stellar metallicity of a galaxy after quenching is the same as when quenching started. However, if star formation in the disc of a galaxy is allowed to continue but accretion of low-metallicity gas is cut off- i.e. the quenching is slow- this balance is upset and the galaxy's gas-phase metallicity is no longer being diluted. Generations of stars formed during slow quenching will be of a higher metallicity than before, and this process continues until the galaxy's gas is exhausted. Under this scenario, the galaxy's stellar metallicity is much higher after quenching than it was before.

T20 and P15 argue that galaxies evolve along the "main sequence" in the SFR-M_* plane and the star forming mass-metallicity relation until slow quenching begins. During quenching, their SFR decreases and their metallicity increases such that they eventually lie in the passive regions of the main sequence and the mass-metallicity relations. This evolution leads to vertical or nearly vertical tracks in the mass-metallicity plane, as a large increase in metallicity is accompanied by only a small increase in stellar mass (P15; T20).

Our findings raise questions about this interpretation. Firstly, Figure 3 shows the importance of having robust size measurements for each galaxy. The near vertical motion in the mass-metallicity plane proposed by P15 and T20 must *also* be accompanied by a decrease in size for the galaxy undergoing quenching to remain on the [Z/H]-Φ plot from Figure 3 (as long as the assumption of a constant relation between [Z/H] and Φ is valid: see Section 6.3).

For an increase in metallicity of 0.2 dex and no change in stellar mass, the right panel of Figure 3 implies that the value of $\log_{10}\left(\frac{M_*}{M_\odot}\right) - \log_{10}\left(\frac{r_e}{\text{kpc}}\right)$ of the galaxy must change by $\approx$0.4 dex. For no change in stellar mass, the half-light radius of a galaxy must therefore *decrease* by 0.4 dex (i.e. end up at $\sim$40% of its value before quenching began). Such a reduction in size is not found in simulations of individual galaxies undergoing slow quenching (e.g. Genel et al. 2018), nor in the recent study of Croom et al. 2021b who investigated the effects of disk-fading on star-forming galaxies and found a reduction in r_e of $\approx$ 10% (0.05 dex). Moreover, a number of studies have found that recently quenched galaxies tend to have large radii (i.e. radii similar to star-forming galaxies) when they join the passive population (e.g. Cassata et al. 2013; Carollo et al. 2013; Krogager et al. 2014; Cortese et al. 2019).

6.2 Quenching toy models

We now investigate whether we can reproduce our observations using toy models of galaxy quenching. The aim of this Section is to investigate whether a model with almost instantaneous quenching- rather than the slow quenching advocated by P15 and T20- can simultaneously account for the distribution of galaxies in the mass-metallicity, [Z/H]-Φ and mass-size planes.

We build a simple model where star-forming galaxies grow in mass and size and evolve in metallicity as they accrete gas and form new stars. These galaxies then have a probability to quench at the
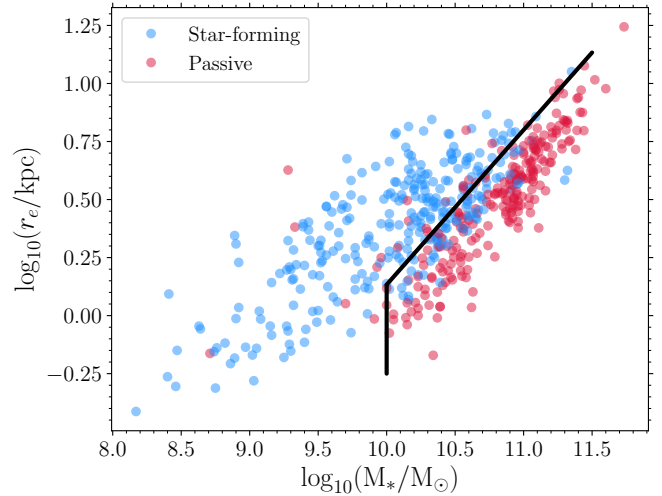

Figure 5. The mass-size plane of the central and isolated galaxies in our sample. Star-forming galaxies are shown in blue and quenched galaxies are shown in red. When a galaxy in our toy model crosses the thick black line as it grows in mass and size, we assign it a 5% probability of quenching during the next time step (see Section 6.2 for details).

start of each timestep, with this probability (p_{quench}) depending on a combination of their mass and their size. Once galaxies become quenched, they stop their evolution and fix their values of mass, size and metallicity until redshift zero.

We begin by assigning a formation redshift to each galaxy, which is drawn from a uniform distribution between one and six. We next assign galaxies a stellar mass. We use the results from Davidzon et al. (2017), who study the galaxy stellar mass function of star-forming and passive galaxies out to redshift six. We use the results from their "active sample" to draw stellar masses from a double Schechter function at $z \leq 3$ and a single Schechter function at $z > 3$. These represent star-forming galaxies.

We then place galaxies on the mass-size relation for star-forming galaxies at the redshift of their formation, using measurements from van der Wel et al. (2014). Next, we must assign each galaxy a stellar metallicity. Measurements of the mass-metallicity relation at high redshift are currently limited to studies of ionised gas emission lines. We therefore make a further assumption; that the [Z/H]-Φ relationship is the same at high-redshift as it is at low redshift (i.e. that measured in Section 5). This assumption is unlikely to be completely correct, and we discuss its validity in Section 6.3.

We are then left with two free parameters; the intercept of [the Z/H]-Φ relationship relationship and the intrinsic scatter around it. We choose an intercept of 0.03 dex to match the "combined" relation from Table 1, and an intrinsic scatter of 0.08 dex.

Galaxies are evolved forward in time using a timestep of 100 Myr, from their formation redshift to today. To set the amount of stellar mass formed at each timestep, we place star-forming galaxies on the main sequence of star-formation at the appropriate redshift, using the "consensus" relation from Speagle et al. (2014). Furthermore, galaxies grow in metallicity according to the "combined" relation described in Section 5. Galaxies increase in size according to:

$$\delta \log R = 0.3 \delta \log M_* \tag{7}$$

This evolution in size as a function of mass has been measured by recent observational studies (e.g. van Dokkum et al. 2013, and
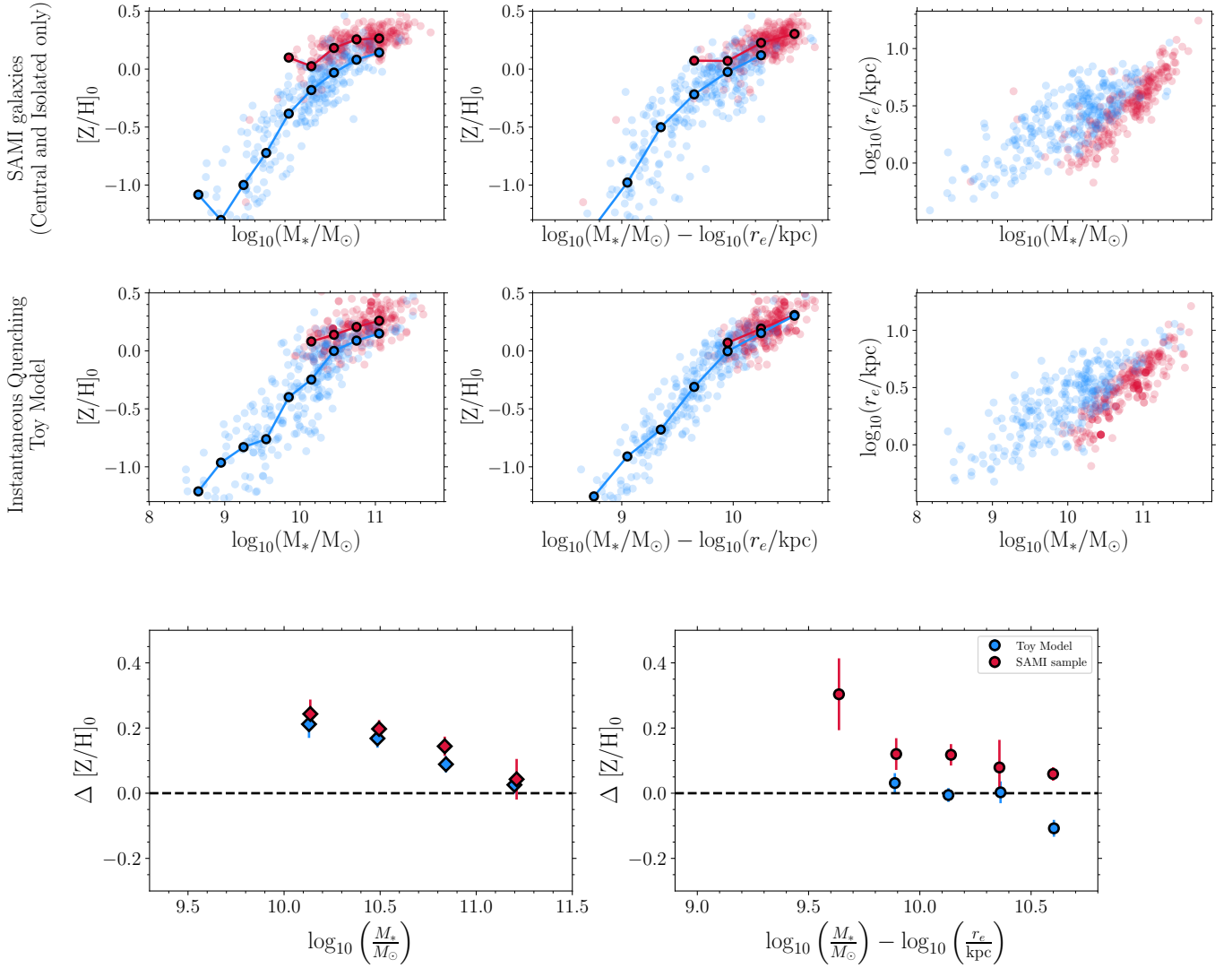
Figure 6. A comparison between the data from our sample of SAMI central and isolated galaxies (top row) to simulated galaxies from our toy model of instantaneous quenching (middle row). The columns show the [Z-H]-M_* relation (left), the [Z-H]-Φ relation (middle) and the mass-size relation (right). The bottom row shows the difference in metallicity between passive and star-forming galaxies as a function of mass (left) and Φ (right), for the SAMI sample (red points) and the galaxies from the toy model (blue points). We find a very good quantitative agreement between the two samples; in particular, we recover the mass-dependent offset in [Z/H] between passive and star-forming galaxies in our model with instantaneous quenching. We note that the agreement between the model and data in the mass-size panel is by construction; we have sampled our model galaxies to have the same mass and size functions as the SAMI data

. Overall, this model implies that the difference in metallicity between star-forming and passive galaxies at fixed mass cannot, in isolation, be used as evidence of slow quenching.

references therein) as well as in simulations (Zolotov et al. 2015). Other studies find slightly different values (e.g. $\delta \log R \approx 0.4\delta \log M_*$ in Hirschmann et al. 2013, $\delta \log R \approx 0.4\delta \log M_*$ in Genel et al. 2018) but small changes to this value do not affect our conclusions.

The final piece is the inclusion of quenching. Figure 5 shows the mass-size plane of the galaxies in our central-only sample. A thick black line shows the region containing the majority of the quenched galaxies in the sample. This region is bounded by:

(i) $\log_{10}(M_*/M_\odot) = 10$, a line of constant stellar mass.
(ii) $\log_{10}(M_*/M_\odot) - \frac{3}{2}\log_{10}(r_e/\mathrm{kpc}) = 9.8$

In the model, if a galaxy grows in mass and size such that it crosses to the right of the line in the mass-size plane, it is assigned a probability of quenching of $p_{\mathrm{quench}} = 0.05$ at all future timesteps.

Galaxies outside the shaded region have $p_{\mathrm{quench}} = 0$. This value of $p_{\mathrm{quench}} = 0.05$ was chosen to give a good match between the quenched fraction of the final simulated galaxies and the quenched fraction in the SAMI central-only sample.

At the start of each timestep, we draw a random number on the unit interval and compare with p_{quench} to decide whether a given galaxy continues to form stars or becomes quenched. If the galaxy quenches at a given timestep, it stops evolving completely in mass, size and metallicity; its values of these quantities at the onset of quenching are frozen in place until redshift zero. This model of galaxy quenching is effectively instantaneous (i.e. completely shutting down star-formation on a timescale of 100 Myrs), unlike the slow quenching (on timescales of Gyrs) discussed in P15 and T20. We note that our choice of $p_{\mathrm{quench}} = 0.05$ per timestep implies that a galaxy in

Table 2. A comparison of the straight-line fits to the mass-metallicity relation for the SAMI centrals and instantaneous quenching toy model shown in Figure 6. We fit a relation of the form $[Z/H] = m(\log_{10}(M_*/M_\odot) - 10.3) + c$. The toy model reproduces the mass-metallicity relation of the SAMI centrals almost exactly.

	$c_{\text{star-forming}}$	c_{passive}	$m_{\text{star-forming}}$	m_{passive}
SAMI centrals	-0.15 ± 0.01	0.12 ± 0.01	0.61 ± 0.03	0.21 ± 0.02
Toy model	-0.18 ± 0.02	0.09 ± 0.01	0.65 ± 0.02	0.24 ± 0.02

the shaded region of the mass-size plane has a $\approx 40\%$ chance of quenching after 1 Gyr (10 timesteps).

We create 10^4 galaxies and evolve them forwards from their initial redshifts to today. We then compare quantitatively to the central-only SAMI sample discussed in Section 3, in order to minimise the effects of environmental quenching processes which are not included in our model. This central-only sample contains 527 galaxies. We then randomly sample 527 galaxies from our toy model with the same mass function and size distribution as our SAMI galaxies. Finally, we add reasonable measurement uncertainties to our final model values; a 0.1 dex scatter in stellar mass and a 0.05 dex scatter in [Z/H] and size.

6.2.1 Results from our model

Our results are shown in Figure 6. The top row shows the observed SAMI central and isolated galaxies and the middle row shows results from our instantaneous quenching model. We plot three important relationships: the mass-metallicity relation in the first column; the [Z/H]-Φ relation in the second panel; and the mass-size relation in the third panel.

We find that this very simple model can produce an offset in stellar metallicity between star-forming and quiescent galaxies at fixed mass, implying that slow quenching is not the only way to produce this. Our instantaneous quenching model recovers a difference of 0.27 dex between the metallicity of passive and star-forming galaxies at a mass of $\log_{10}(M_*/M_\odot) = 10.3$, identical to that from the central-only sample. The existence of this metallicity gap was used by P15 and T20 to conclude that most galaxies undergo slow quenching processes, but this work shows that such a gap can exist even when quenching is nearly instantaneous. In the bottom panel of of Figure 6, we also show that we recover the change in this offset as a function of mass in our model.

We also note that the model does a good job of recovering the over-all quenched fraction of galaxies, as well as the quenched fraction of galaxies as a function of mass. In this sample of SAMI centrals, 53% of galaxies are quenched, compared to the 47% of galaxies in our toy model which are quiescent. Figure 7 shows the distribution of quenched (red points) and star-forming (blue points) galaxies against stellar mass in the model (left panel) and in the SAMI data (middle panel). The black points show the fraction of galaxies that are quenched in mass bins of width 0.25 dex.

We perform logistic regression on the SAMI galaxies and the model galaxies, using their stellar mass as an input and whether they are quenched or star-forming as the binary dependent variable. These are shown by the curved lines in each panel. This is simply another way to compare the quenched fractions as a function of mass between the model and the data. Both the binned fractions and logistic curves show that the model and the data agree well.

In Figure 8 we show the mass-metallicity relation of our SAMI sample with each point coloured by its effective radius. On the right,

we present the same plot for our simulated galaxies. The two panels are in excellent agreement, both showing a clear trend with radius across the relation (see also Barone et al. 2018 and Barone et al. 2020 who show the same result for early and late type galaxies separately). We note that in all areas of the mass-metallicity plane, at fixed mass galaxies which are smaller have higher metallicity. This is not only true at the high-mass end, where the quenched and star-forming galaxies are offset from one another (as shown in Figure 3), but for star-forming galaxies at lower masses too. We return to this point in Section 6.5.1 to discuss what we can learn about the reason behind the offset in [Z/H] between quenched and star-forming galaxies.

Finally, we can see from the bottom panel of Figure 6 that our model underpredicts the offset in [Z/H] as a function of Φ by a small amount: the average $\Delta[Z/H]$ is 0.1 dex for the SAMI sample (0.08 dex if we remove the first outlying point) and -0.02 dex for the toy model galaxies (0.01 dex if we remove the final negative value). This may be pointing to the fact that a process like slow quenching via strangulation, where a galaxy increases its [Z/H] without large changes in $\log_{10}(M_*/M_\odot)$ and r_e, is needed. If all galaxies increase their [Z/H] by ≈ 0.05-0.1 dex when they quench, without changing in mass or radius, we would retain the agreement in the mass-metallicity plane whilst getting a better match between model and data in the [Z/H]-Φ plane. We note, however, that this is a smaller increase in metallicity due to slow quenching than proposed by P15 and T20.

6.3 Is the [Z/H]-Φ relation constant with redshift?

In our model, we made the simplifying assumption that the relationship between [Z/H] and Φ measured in Section 5 is the same at all redshifts. Since the relationship between [Z/H] and Φ has not been studied in a comparable manner at higher redshifts, assuming that it is constant over cosmic time is the simplest assumption to make without complicating our toy model by parameterising its evolution. As we have shown, making this assumption combined with a specific model of quenching, allows us to recover the [Z/H]-M_* and [Z/H]-Φ relations of our sample.

However, the assumption of a constant relationship between [Z/H] and Φ is unlikely to be correct, as the following simple argument below shows. At a given mass, galaxies at high redshift are smaller than those at $z = 0$ (e.g. van der Wel et al. 2014). This means that these high-redshift galaxies would have a larger value of Φ than their mass-matched counterparts at redshift zero. We also know that the mass-metallicity relationship evolves with redshift, for both star-forming (e.g. Cullen et al. 2019; Kashino et al. 2022) and quiescent galaxies (e.g. Leethochawalit et al. 2018, 2019), with high redshift galaxies being more metal poor than today. Taken together, these facts imply that the relationship between [Z/H] and Φ must be shifted both downwards and to the right of the $z = 0$ result from Section 5.

It is beyond the scope of this paper to further complicate our simple model by including evolution of the [Z/H]-Φ relation over cosmic time. We encourage simulators to study this relationship in their work (e.g. by studying [Z/H] in cosmological simulations; see e.g Guo et al. 2016, De Rossi et al. 2017, or use semi-analytic models which track stellar metallicity (e.g. SHARK; Lagos et al. 2018) to investigate whether they recover the results found in this work.

A key point to make here is that chemical evolution (i.e. an increase in metallicity) during quenching is intentionally ignored in the model, whilst on the other hand it is clear that that such evolution will undoubtedly take place for the vast majority of galaxies (those which quench on timescales longer than a few Myrs).

The larger the evolution in the [Z/H]-Φ relation (i.e. the greater departure from the assumption in this work), the greater the need for
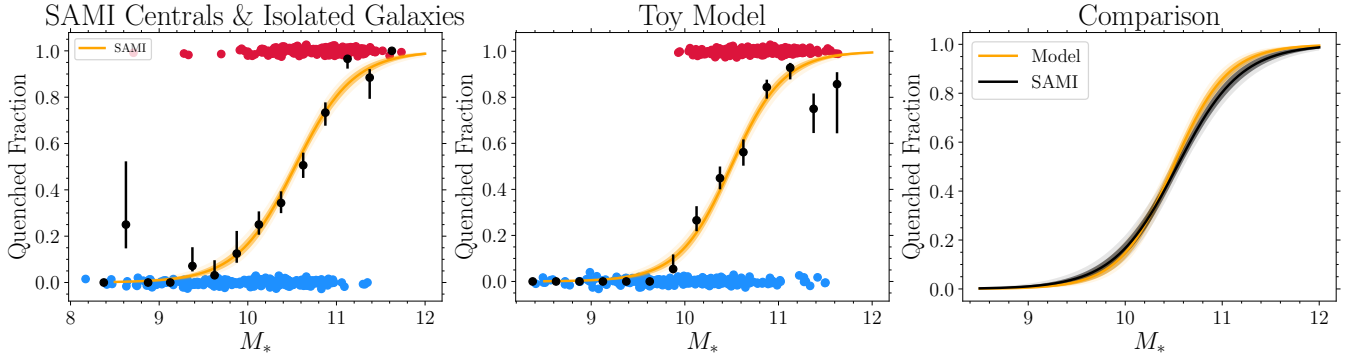
Figure 7. The quenched fraction of galaxies in our our sample of SAMI centrals (left) and our toy model of quenching (middle). We show whether galaxies are passive (red points, plotted at a y value around 1) or star-forming (blue points, at a y value around 0.0) as a function of their stellar mass. The points have had a small random jitter added such that they don't all lie on top of one another. Black points with error bars show the quenched fraction of galaxies in each bin of stellar mass. The curved lines show logistic regression fits to the same data, with the shaded regions highlighting the $1-\sigma$ uncertainty. The right panel compares the logistic regression fits for the SAMI centrals (black) and the model galaxies (orange), showing the good agreement between the two.

galaxies to increase their metallicity via chemical evolution during quenching, as discussed by P15 and T20. A key topic for future work will therefore be to measure the stellar metallicity, mass and size of galaxies at intermediate and high redshift in order to pin down this evolution (see e.g. Barone et al. 2022).

6.4 Comparison with previous work

A number of previous studies have investigated quenching on populations of galaxies based on their evolution in M_* and r_e. These studies tend to fall into two categories: those which have galaxies evolving in the mass size plane before quenching at fixed velocity dispersion, and those which find that galaxies quench at fixed surface density (M_*/r_e^2). van der Wel et al. (2009), Cappellari et al. (2013b), van Dokkum et al. (2015) and Haines et al. (2017) can be broadly grouped into the former category, whilst Tacchella et al. (2015) and Barro et al. (2017) and Barone et al. (2022) belong to the latter.

Chen et al. (2020) take this area of modelling one step further and consider the evolution of galaxies in the four dimensional space of central surface density (Σ_1), M_*, r_e and central black hole mass, $M_\bullet$. Their work used straight lines in the Σ_1-M_* plane which evolves with redshift as a quenching boundary, which they translated to the mass-size plane using the Sérsic indices of quiescent galaxies. Their key insight is showing that this quenching boundary in the Σ_1-M_* plane can be related to the total energy deposited into the galaxy halo by the central black hole. Using such a model, Chen et al. (2020) recover an impressive number of correlations and properties of the galaxy population in the local Universe.

Our study is the first to include stellar metallicity in a quenching model based on mass and size. We also use an "in-between" quenching boundary of $M_*/r_e^{3/2}$, instead of M/r_e or M/r_e^2, since this gives the best match to our observational data.

We investigated a number of different boundaries for the regions where galaxies have a non-zero probability of quenching during their next timestep. A quenching boundary at fixed mass leads to a vertical boundary between quenched and star-forming galaxies in the mass-metallicity plane, and cannot reproduce the fact that quiescent and star-forming galaxies of the same mass are observed. It would also not reproduce the mass-size plane we observe, which has a sloped line separating star-forming and passive galaxies. Similarly, a quenching boundary at fixed M/r is unsatisfactory, since it tends to lead to a

hard vertical line dividing quenched and star-forming galaxies in the [Z/H]-Φ plane. This is not observed in the data, where there is a small overlap between the two populations at $\Phi \approx 10.2$. We also find that a fixed M/r boundary leads to a steep slope in the [Z/H]-M_* plane for the quiescent galaxies, as well as too few quenched galaxies at low mass. This last point means that the quenched fractions as a function of mass in Figure 7 would not be a good match. On the other hand, quenching at a fixed surface density leads to too many low-mass quiescent centrals and a very flat slope in the [Z/H]-M_* plane. We therefore concluded that a compromise worked best; a line of fixed $\log_{10}(M_*/M_\odot)$- $\frac{3}{2}\log_{10}(r_e/\mathrm{kpc})$, which has a slope somewhere between these two lines.

We should stress that this exercise is designed to show that a sensible model using instantaneous quenching can be used to model galaxies in the [Z/H]-M_* plane, and that modelling stellar metallicities in this way can be accomplished by using the relationship between [Z/H] and Φ. We do not aim to conclude that the quenching boundaries in Figure 5 supersede all others, or that this parameterisation of quenching should be taken as exactly what happens in the Universe. It is clear that the parameter space of possible such quenching models is very large, with the possibility of including time varying quenching strengths, different functional forms of quenching probability (e.g. see Peng et al. 2010 and Lilly & Carollo 2016) and/or the inclusion of galaxy mergers and environmental-based quenching. Expanding our simple model in these ways is a topic for future work.

6.5 Implications

We find that our simple model of galaxy quenching which depends on both the mass and size of a galaxy can recover the difference in metallicity between star-forming and quiescent galaxies at fixed mass, implying that such a difference alone cannot be used as evidence of slow quenching processes. This is not to say that processes which remove a galaxy's halo of metal-poor gas are not important quenching pathways; evidence for disk strangulation (and its more extreme cousin ram-pressure stripping) has been found in the local Universe (e.g. Poggianti et al. 2017; Owers et al. 2019 and see Cortese et al. 2021 for a review), at higher redshifts (e.g. Maier et al. 2016, 2019; Vaughan et al. 2020) and in simulations (e.g. De Rossi et al. 2015).

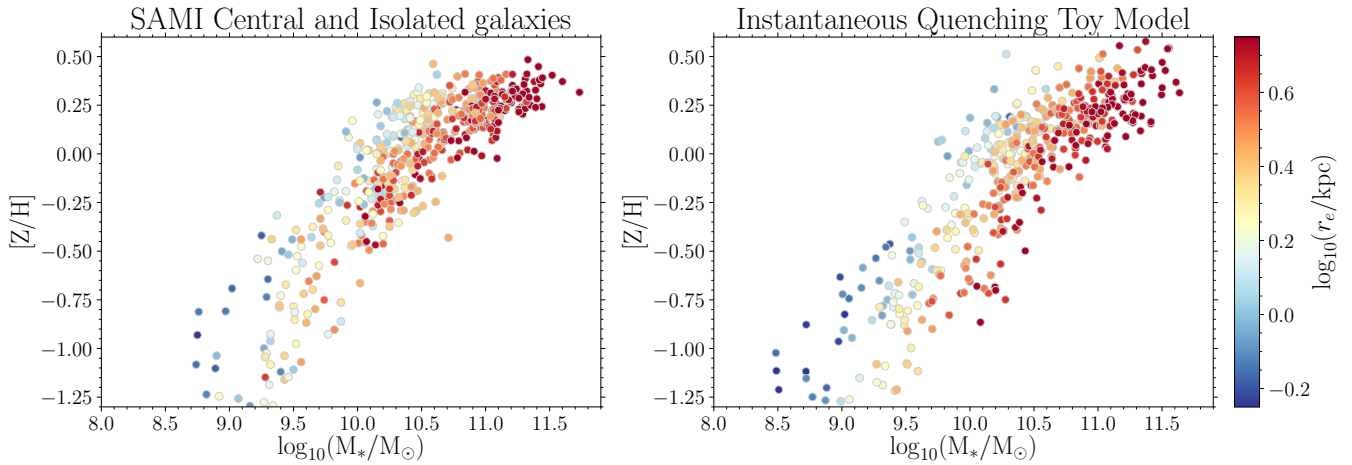Our model also implies that merging processes are not necessarily

Figure 8. Plots of the mass-metallicity relationship for our SAMI galaxies (left) and simulated objects (right), with each point coloured by its effective radius. This figure emphasises that for two galaxies with the same mass, the one with the smaller radius will tend to have the higher metallicity, regardless of whether they are star-forming or quenched.

important in setting the slopes of the mass-size, [Z/H]-M_* and [Z/H]-Φ relations, since we recover these in a model that does not contain any galaxy interactions explicitly[4]. The fact that our toy model of galaxy evolution recovers a number of important results without explicit major merging is perhaps not too surprising, since simulations have suggested that the rate of growth due to major mergers (mass ratio greater than 1:10) contribute only 20% of a galaxy's overall mass growth (Wang et al. 2011; L'Huillier et al. 2012). Whilst major mergers are more important in high-density environments, it is clear that gas accretion from the cosmic web and in-situ star formation is the predominant mass-growth channel for most galaxies in the Universe.

6.5.1 What leads to the difference in [Z/H] between passive and star-forming galaxies?

By tracing the metallicity, mass and size history of the galaxies in our toy model, we can investigate the cause of metallicity difference between quenched and star-forming galaxies at fixed mass.

Figure 9 shows the mass-size plane of simulated galaxies which have been chosen to match our observational sample[5]. For each model galaxy, we plot its trajectory in the mass-size plane from the time it enters our model (i.e. from the starting mass, size and formation redshift it is assigned). Galaxies which are passive at redshift zero are coloured in red, whilst galaxies which are still star-forming are blue.

At any given mass, quenched galaxies tend to have smaller radii than galaxies which are still star-forming (e.g. van der Wel et al. 2014). Figure 9 reinforces that in our model this is (by construction) true at all times in the past: galaxies which end up passive at redshift

zero are (nearly) always smaller than those which end up to be star-forming. This is a simple consequence of the modelling assumptions we have made. Equation 7 implies that all galaxies follow parallel tracks in the mass-size plane whilst they are star-forming, and so the smallest galaxies in a population remain the smallest.

This fact impacts the final metallicities of the galaxy population through our assumption that [Z/H] traces $\Phi = \log_{10}\left(\frac{M_*}{M_\odot}\right) - \log_{10}\left(\frac{r_e}{\mathrm{kpc}}\right)$ at all times in a galaxy's history (and see also Barone et al. (2022) who show that [Z/H] traces Φ in their sample of galaxies at $z = 0.76$). At any given point, galaxies with small radii for their mass will have larger values of Φ, and so will tend to have a larger value of [Z/H]. This is not only true when comparing passive and star-forming objects; as shown in Figure 8, smaller galaxies tend to have higher stellar metallicities even in locations of the diagram where everything is star-forming. Our model implies that this residual size dependence is baked in from a galaxy's formation: objects with higher metallicities at fixed mass have always been the smallest objects for their mass in a population, and it is this fact which leads to their location in the mass-metallicity plane today (e.g. as seen in Figure 8).

Related to this idea is our quenching prescription: galaxies quench once they cross a diagonal boundary in the mass-size plane. By design, this boundary will tend to quench galaxies which are small for their mass and "freeze" their values of mass, size and metallicity in place. Since this prescription does not allow for galaxies to increase their metallicity after quenching, however, it does not contribute to the offset in metallicity at fixed mass between star-forming and passive galaxies (unlike the slow-quenching described in P15 and T20).

7 CONCLUSIONS

This work builds on the studies of Barone et al. (2018), D'Eugenio et al. (2018) and Barone et al. (2020) by investigating the correlation between stellar metallicity ([Z/H]) and $\Phi = \log_{10}\left(\frac{M_*}{M_\odot}\right) - \log_{10}\left(\frac{r_e}{\mathrm{kpc}}\right)$ for a homogeneously-observed sample of galaxies. We use the SAMI galaxy survey to measure central metallicity values

---

[4] It should be noted that we have sampled our simulated galaxies to follow the same mass-size relation as the observed SAMI galaxies, however. If mergers play a role in shaping the observed mass-size relation, they will be implicitly included in our model.

[5] We note that here we are plotting the mass and radius values from the simulation without any "observational" uncertainties applied, unlike in the bottom panel of Figure 6
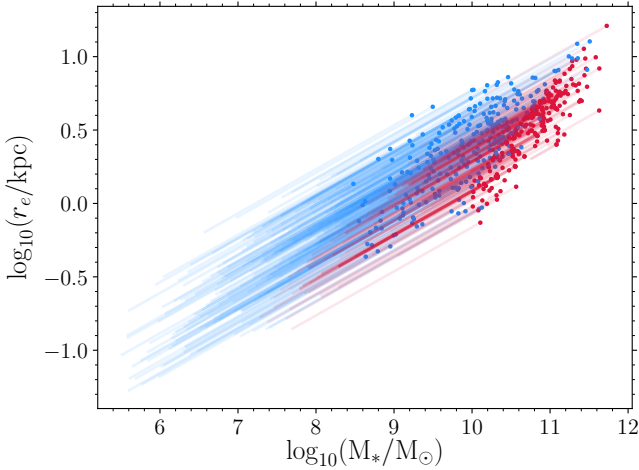
Figure 9. Tracks in the mass-size plane for our simulated galaxies. This plot emphasises that our model galaxies move in parallel in the mass-size plane, and that galaxies which are quiescent at redshift zero have always been amongst the smallest objects for their mass in a population.

for 1363 galaxies which also have robust stellar mass, half-light radius and star-formation rate measurements, and build a simple toy model of galaxy evolution which has galaxies evolving in mass, size and [Z/H] to explain our findings. Galaxies in this model have a probability p_{quench} to undergo nearly instantaneous quenching (from main-sequence to fully passive in under 100 Myrs).

Our findings are as follows:

(i) We recover the well-known offset between the metallicity of star-forming and quiescent galaxies at fixed mass, with our results in very good agreement with the previous work of Peng et al. (2015) and Trussler et al. (2020).

(ii) We show for the first time that star-forming, passive and intermediate ("green valley") galaxies form a single sequence in the [Z/H]-Φ relation, with passive galaxies preferentially being found to the right of the plot (at larger values of Φ).

(iii) The difference in metallicity between passive and star-forming galaxies is smaller at fixed Φ than at fixed $\log_{10}(M_*/M_\odot)$. At fixed Φ, Δ[Z/H] is ≈ 0.1 dex for all values of Φ. This is smaller than or equal to the difference between star-forming and passive galaxies at fixed mass, which ranges from ≈ 0.1 dex at high masses and up to ≈ 0.35 dex below $\log_{10}(M_*/M_\odot)=10$.

(iv) In our toy model of galaxy evolution with instantaneous quenching, choosing a quenching probability which depends on a galaxy's mass *and size* allows us to quantitatively recover the slope of the [Z/H]-M_* relation for our sample, as well as account for the offset in metallicity between star-forming and passive galaxies at fixed mass. We therefore conclude that this offset is not necessarily the result of slow quenching, in contrast to the studies of Peng et al. (2015) and Trussler et al. (2020).

(v) We do find that our toy model slightly underpredicts the difference in metallicity between star-forming and passive galaxies at fixed Φ by ≈ 0.05 dex. If galaxies increase in metallicity by ≈ 0.03–0.05 dex whilst quenching (e.g. during the processes discussed in P15 and T20), our model would retain the good agreement in the mass-metallicity plane whilst giving a closer match in the [Z/H]-Φ plane. We note, however, that this amount of slow quenching is much less than P15 and T20 propose.

This study adds to the collection of work which shows the importance of accounting for galaxy size when investigating stellar populations, and not only considering stellar mass. Future work to investigate the [Z/H] properties of galaxies at higher redshifts (e.g in the forthcoming MAGPI survey; Foster et al. 2020), as well as in nearby low-mass galaxies and comparing to cosmological simulations, will be invaluable to understand the relationship between galaxy mass, size and stellar metallicity.

DATA AVAILABILITY

The observations used in this work have been released as part of the SAMI Data Release 3 (Croom et al. 2021a). The metallicity measurements used in this article will be shared on reasonable request to the corresponding author.

REFERENCES

Abadi M. G., Moore B., Bower R. G., 1999, MNRAS, 308, 947
Abazajian K. N., et al., 2009, ApJS, 182, 543
Ahn C. P., et al., 2012, ApJS, 203, 21
Astropy Collaboration et al., 2013, A&A, 558, A33
Baldwin C., McDermid R. M., Kuntschner H., Maraston C., Conroy C., 2018, MNRAS, 473, 4698
Barat D., et al., 2019, MNRAS, 487, 2924
Barat D., D'Eugenio F., Colless M., Sweet S. M., Groves B., Cortese L., 2020, MNRAS, 498, 5885
Barone T. M., et al., 2018, ApJ, 856, 64
Barone T. M., D'Eugenio F., Colless M., Scott N., 2020, ApJ, 898, 62
Barone T. M., et al., 2022, MNRAS, 512, 3828
Barro G., et al., 2017, ApJ, 840, 47
Bell E. F., de Jong R. S., 2001, ApJ, 550, 212
Bland-Hawthorn J., et al., 2011, Optics Express, 19, 2649
Blanton M. R., et al., 2017, AJ, 154, 28
Bryant J. J., Bland-Hawthorn J., Fogarty L. M. R., Lawrence J. S., Croom S. M., 2014, MNRAS, 438, 869
Bryant J. J., et al., 2015, MNRAS, 447, 2857
Byrne C. M., Stanway E. R., Eldridge J. J., McSwiney L., Townsend O. T., 2022, MNRAS, 512, 5329
Cappellari M., 2002, MNRAS, 333, 400
Cappellari M., 2017, MNRAS, 466, 798
Cappellari M., Copin Y., 2003, MNRAS, 342, 345
Cappellari M., Emsellem E., 2004, PASP, 116, 138
Cappellari M., et al., 2013a, MNRAS, 432, 1862
Cappellari M., et al., 2013b, MNRAS, 432, 1709
Carollo C. M., et al., 2013, ApJ, 773, 112
Carpenter B., et al., 2017, Journal of Statistical Software, 76
Cassata P., et al., 2013, ApJ, 775, 106
Chabrier G., 2003, PASP, 115, 763
Chen Z., et al., 2020, ApJ, 897, 102
Conroy C., 2013, ARA&A, 51, 393
Cortese L., et al., 2019, MNRAS, 485, 2656
Cortese L., Catinella B., Smith R., 2021, Publ. Astron. Soc. Australia, 38, e035
Croom S. M., et al., 2012, MNRAS, 421, 872
Croom S. M., et al., 2021a, MNRAS,
Croom S. M., et al., 2021b, MNRAS, 505, 2247
Cullen F., et al., 2019, MNRAS, 487, 2038
D'Eugenio F., Colless M., Groves B., Bian F., Barone T. M., 2018, MNRAS, 479, 1807
D'Eugenio F., et al., 2021, MNRAS,
Davidzon I., et al., 2017, A&A, 605, A70
De Rossi M. E., Theuns T., Font A. S., McCarthy I. G., 2015, MNRAS, 452, 486
De Rossi M. E., Bower R. G., Font A. S., Schaye J., Theuns T., 2017, MNRAS, 472, 3354
Dekel A., Birnboim Y., 2006, MNRAS, 368, 2
Di Matteo T., Springel V., Hernquist L., 2005, Nature, 433, 604
Eisenstein D. J., et al., 2011, AJ, 142, 72
Eldridge J. J., Stanway E. R., Xiao L., McClelland L. A. S., Taylor G., Ng M., Greis S. M. L., Bray J. C., 2017, Publ. Astron. Soc. Australia, 34, e058
Eminian C., Kauffmann G., Charlot S., Wild V., Bruzual G., Rettura A., Loveday J., 2008, MNRAS, 384, 930
Emsellem E., Bacon R., Monnet G., Poulain P., 1996, A&A, 312, 777
Fan Z., de Grijs R., Chen B., Jiang L., Bian F., Li Z., 2016, AJ, 152, 208
Foster C., et al., 2020, arXiv e-prints, p. arXiv:2011.13567

Franx M., Illingworth G., 1990, ApJ, 359, L41
Gallazzi A., Charlot S., Brinchmann J., White S. D. M., Tremonti C. A., 2005, MNRAS, 362, 41
Ge J., Mao S., Lu Y., Cappellari M., Yan R., 2019, MNRAS, 485, 1675
Gelman A., Rubin D. B., 1992, Statistical Science, 7, 457
Gelman A., Carlin J., Stern H., Dunson D., Vehtari A., Rubin D., 2013, Bayesian Data Analysis, Third Edition. Chapman & Hall/CRC Texts in Statistical Science, Taylor & Francis, https://books.google.com.au/books?id=ZXL6AQAAQBAJ
Genel S., et al., 2018, MNRAS, 474, 3976
Goddard D., et al., 2017, MNRAS, 465, 688
González Delgado R. M., Cid Fernandes R., 2010, MNRAS, 403, 797
Graves G. J., Faber S. M., Schiavon R. P., 2009a, ApJ, 693, 486
Graves G. J., Faber S. M., Schiavon R. P., 2009b, ApJ, 698, 1590
Grumitt R. D. P., Jew L. R. P., Dickinson C., 2020, MNRAS, 496, 4383
Gunn J. E., Gott J. Richard I., 1972, ApJ, 176, 1
Guo Q., et al., 2016, MNRAS, 461, 3457
Haines C. P., et al., 2017, A&A, 605, A4
Hirschmann M., et al., 2013, MNRAS, 436, 2929
Hoffman M. D., Gelman A., 2014, Journal of Machine Learning Research, 15, 1593
Hunter J. D., 2007, Computing In Science & Engineering, 9, 90
Kashino D., et al., 2022, ApJ, 925, 82
Kormendy J., Kennicutt Robert C. J., 2004, ARA&A, 42, 603
Krogager J. K., Zirm A. W., Toft S., Man A., Brammer G., 2014, ApJ, 797, 17
L'Huillier B., Combes F., Semelin B., 2012, A&A, 544, A68
Lagos C. d. P., Tobar R. J., Robotham A. S. G., Obreschkow D., Mitchell P. D., Power C., Elahi P. J., 2018, MNRAS, 481, 3573
Lange R., et al., 2015, MNRAS, 447, 2603
Larson R. B., Tinsley B. M., Caldwell C. N., 1980, ApJ, 237, 692
Lee H.-c., Worthey G., Trager S. C., Faber S. M., 2007, ApJ, 664, 215
Leethochawalit N., Kirby E. N., Moran S. M., Ellis R. S., Treu T., 2018, ApJ, 856, 15
Leethochawalit N., Kirby E. N., Ellis R. S., Moran S. M., Treu T., 2019, ApJ, 885, 100
Li H., et al., 2018, MNRAS, 476, 1765
Lieu M., Farr W. M., Betancourt M., Smith G. P., Sereno M., McCarthy I. G., 2017, MNRAS, 468, 4872
Lilly S. J., Carollo C. M., 2016, ApJ, 833, 1
Magorrian J., et al., 1998, AJ, 115, 2285
Maier C., et al., 2016, A&A, 590, A108
Maier C., Ziegler B. L., Haines C. P., Smith G. P., 2019, A&A, 621, A131
McDermid R. M., et al., 2015, MNRAS, 448, 3484
Medling A. M., et al., 2018, MNRAS, 475, 5194
Mölder F., et al., 2021, F1000Research, 10
Nelan J. E., Smith R. J., Hudson M. J., Wegner G. A., Lucey J. R., Moore S. A. W., Quinney S. J., Suntzeff N. B., 2005, ApJ, 632, 137
Noeske K. G., et al., 2007, ApJ, 660, L43
Owers M. S., et al., 2019, ApJ, 873, 52
Peng Y.-j., et al., 2010, ApJ, 721, 193
Peng Y., Maiolino R., Cochrane R., 2015, Nature, 521, 192
Perez F., Granger B. E., 2007, Computing in Science Engineering, 9, 21
Pietrinferni A., Cassisi S., Salaris M., Castelli F., 2004, ApJ, 612, 168
Pietrinferni A., Cassisi S., Salaris M., Castelli F., 2006, ApJ, 642, 797
Poggianti B. M., et al., 2017, ApJ, 844, 48
Renzini A., Peng Y.-j., 2015, ApJ, 801, L29
Robotham A. S. G., et al., 2011, MNRAS, 416, 2640
Santucci G., et al., 2020, ApJ, 896, 75
Schawinski K., et al., 2014, MNRAS, 440, 889
Scott N., et al., 2009, MNRAS, 398, 1835
Scott N., et al., 2017, MNRAS, 472, 2833
Sellwood J. A., 2014, Reviews of Modern Physics, 86, 1
Shanks T., et al., 2015, MNRAS, 451, 4238
Sharp R., et al., 2006, in McLean I. S., Iye M., eds, Society of Photo-Optical Instrumentation Engineers (SPIE) Conference Series Vol. 6269, Society of Photo-Optical Instrumentation Engineers (SPIE) Conference Series. p. 62690G (arXiv:astro-ph/0606137), doi:10.1117/12.671022

Shen S., Mo H. J., White S. D. M., Blanton M. R., Kauffmann G., Voges W., Brinkmann J., Csabai I., 2003, MNRAS, 343, 978

Silk J., Rees M. J., 1998, A&A, 331, L1

Skelton R. E., et al., 2014, ApJS, 214, 24

Smith R. J., et al., 2010, MNRAS, 408, 1417

Speagle J. S., Steinhardt C. L., Capak P. L., Silverman J. D., 2014, ApJS, 214, 15

Stanway E. R., Eldridge J. J., 2018, MNRAS, 479, 75

Suess K. A., Kriek M., Price S. H., Barro G., 2019, ApJ, 885, L22

Tacchella S., et al., 2015, Science, 348, 314

Taylor E. N., et al., 2011, MNRAS, 418, 1587

Thomas D., Maraston C., Bender R., Mendes de Oliveira C., 2005, ApJ, 621, 673

Tinsley B. M., 1968, ApJ, 151, 547

Trager S. C., Faber S. M., Worthey G., González J. J., 2000, AJ, 120, 165

Trussler J., Maiolino R., Maraston C., Peng Y., Thomas D., Goddard D., Lian J., 2020, MNRAS, 491, 5406

Van Rossum G., Drake Jr F. L., 1995, Python reference manual. Centrum voor Wiskunde en Informatica Amsterdam

Varidel M. R., et al., 2020, MNRAS, 495, 2265

Vaughan S. P., et al., 2020, MNRAS, 496, 3841

Vazdekis A., et al., 2015, MNRAS, 449, 1177

Virtanen P., et al., 2020, Nature Methods, 17, 261

Wang J., et al., 2011, MNRAS, 413, 1373

Wes McKinney 2010, in Stéfan van der Walt Jarrod Millman eds, Proceedings of the 9th Python in Science Conference. pp 56 – 61, doi:10.25080/Majora-92bf1922-00a

Woo J., Ellison S. L., 2019, MNRAS, 487, 1927

Woo J., Dekel A., Faber S. M., Koo D. C., 2015, MNRAS, 448, 237

Woo J., Carollo C. M., Faber S. M., Dekel A., Tacchella S., 2017, MNRAS, 464, 1077

York D. G., et al., 2000, AJ, 120, 1579

Zheng Z., et al., 2017, MNRAS, 465, 4572

Zolotov A., et al., 2015, MNRAS, 450, 2327

van Dokkum P. G., et al., 2013, ApJ, 771, L35

van Dokkum P. G., et al., 2015, ApJ, 813, 23

van de Sande J., Kriek M., Franx M., Bezanson R., van Dokkum P. G., 2015, ApJ, 799, 125

van de Sande J., et al., 2017, MNRAS, 472, 1272

van der Walt S., Colbert S. C., Varoquaux G., 2011, Computing in Science Engineering, 13, 22

van der Wel A., Bell E. F., van den Bosch F. C., Gallazzi A., Rix H.-W., 2009, ApJ, 698, 1232

van der Wel A., et al., 2014, ApJ, 788, 28

APPENDIX A: UNCERTAINTIES IN [Z/H]

We require an estimate of the uncertainty in our [Z/H] measurements from each individual Voronoi-binned spectrum. However, running a bootstrap analysis using 50 bootstraps on all 78,531 spectra would take approximately 2.5 years of CPU time and be an unnecessary waste of supercomputer resources and energy. Instead, we bootstrap a subsample of $\approx 10^3$ spectra and use their measured uncertainties to build a model to predict the uncertainty of the remaining spectra.

We carefully select this subsample to span the entire range of S/N and [Z/H] values in our data. We note that selecting a random sample of spectra to bootstrap would *not* be appropriate. Since the majority of our spectra are around solar metallicity, bootstapping a random sample would necessarily lead to a poor prediction of the uncertainties for low-metallicity spectra.

We divide the S/N and [Z/H] plane of our spectra into a 30x30 grid. We select 20 spectra at random from each grid cell, and all the spectra in a grid cell if there are fewer than 20. The two-dimensional histogram of the S/N and [Z/H] properties of the spectra selected for bootstrapping are shown in Figure A1, as well as the distribution of
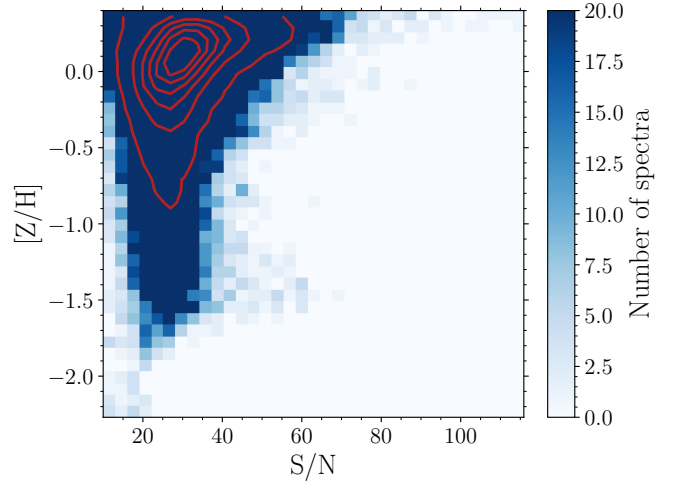

Figure A1. The distribution of [Z/H] and S/N values of the spectra in our sample. The colormap shows the number of spectra from each grid cell chosen for bootstrapping. We select all spectra in each cell unless there are more than 20, in which case we choose a random subsample of 20 spectra. The red contours show the distribution of spectra in the full sample.

the entire sample. Our final bootstrapping sample contains 10,814 spectra.

For each spectrum in the bootstrapping sample, we take the best fitting template from PPXF and add Gaussian random noise at each pixel. This random noise is scaled appropriately by the variance spectrum of the observed data, multiplied by the reduced χ^2 value from the PPXF fit. We then re-fit this spectrum with pPXF and measure the stellar population parameters. This process is repeated 50 times per spectrum.

We aim to predict the bootstrapped uncertainty, $\sigma_{[Z/H]}$, of a spectrum from its S/N and [Z/H] values. To assess the success of our model, we hold back a "test set" of 20% of the data (2163 spectra) and use the remaining 80% to fit to.

As shown in Figure A2, the dependence of $\log_{10}(\sigma_{[Z/H]})$ with [Z/H] is roughly linear for spectra with [Z/H] above -0.5, but becomes approximately flat with [Z/H] below this value. As expected, higher S/N spectra have smaller uncertainties. We note that the colormap has been smoothed using the loess2d algorithm described in Cappellari et al. (2013a)

We therefore capture this behaviour with a simple broken line model. Defining $y = \log_{10}(\sigma_{[Z/H]})$ and $s = \log_{10}(S/N)$, the model has 6 free parameters:

(i) m_1, the dependence of y on s
(ii) z_b, the breakpoint in the y-[Z/H] relationship.
(iii) m_2, the dependence of y on [Z/H] for [Z/H] $\geq z_b$
(iv) m_3, the dependence of y on [Z/H] for [Z/H] $<z_b$
(v) a, the intercept
(vi) τ, the intrinsic scatter around the relation

and is described by the following equation:

$$y = \begin{cases} a + m_1 s + m_2 [Z/H] & \text{if } [Z/H] \geq z_b \\ a + m_1 s + m_3 [Z/H] + (m_3 - m_2)z_b & \text{if } [Z/H] < z_b \end{cases} \quad (A1)$$

Our results are summarised in Table A1. The standard deviation of the residuals between the metallicity uncertainty of the test set and the metallicity uncertainty predicted by the model (where both
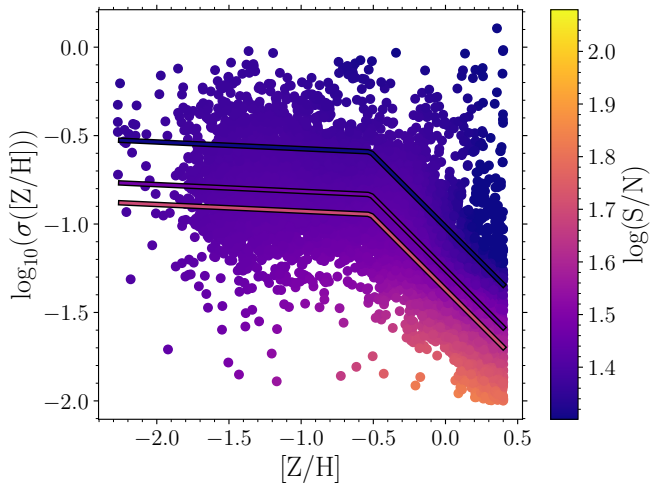
Figure A2. A plot of the bootstrapped uncertainty ($\log_{10}(\sigma_{[Z/H]})$) against the metallicity of each spectrum. The colourbar corresponds to $\log_{10}(S/N)$ of the spectrum, and has been smoothed using the `loess2d` locally-weighted regression algorithm described in Cappellari et al. (2013a).

values are on the log scale) is 0.24 dex, corresponding to us being able to estimate the true uncertainty of a spectrum to better than a factor of 2. The standard deviation on the linear scale (i.e. in terms of $\sigma_{[Z/H]}$) is 0.09 dex.

APPENDIX B: USING A DIFFERENT SET OF SSP MODELS

In this section, we investigate the affect of using a different set of SSP models to measure the stellar metallicity of our sample. We randomly select 130 galaxies from the full sample (approximately 10%, corresponding to 5939 Voronoi bins) and use pPXF to fit version 2.2.1 of the Binary Population and Spectral Synthesis (BPASS) models (Eldridge et al. 2017; Stanway & Eldridge 2018; Byrne et al. 2022) to their spectra. These BPASS templates have an $[\alpha/Fe]$ ratio of 0.0 and use a Chabrier initial mass function (Chabrier 2003). We also only use the "single star" templates, which do not include the effect of binary stars on the final SSP spectra, to more closely match the MILES models. We perform the fit using 228 templates which form a grid in age and metallicity, spanning from 6 Myrs to 15.8 Gyrs in age and from -4.3 to +0.3 in [Z/H]. pPXF is used to perform the fit, with the same settings as in Section 3.

Figure B1 shows the derived mass-metallicity and Φ-metallicity relations. We see that measurements with the BPASS models are offset to lower values of metallicity, with the difference being as large as 1 dex in the most discrepant cases at high values of mass or Φ.

The fact that two different SSP models do not precisely agree on the absolute values of metallicity in a spectrum is not particularly surprising, since finding differences in the recovery of stellar population parameters when using different SSP models is well known (e.g. González Delgado & Cid Fernandes 2010; Fan et al. 2016; Baldwin et al. 2018; Ge et al. 2019). Whilst a full investigation of the reasons behind the different derived metallicities from the MILES and BPASS models is beyond the scope of this paper, we note the large number of different ingredients between the two; the models use different isochrones (the BaSTI isochrones for MILES, a custom stellar evolutionary prescription described in Eldridge et al. (2017)

for BPASS), different stellar libraries (empirical stellar spectra for MILES, theoretical model atmospheres for BPASS) and have a different high-mass cutoff for the assumed IMF (100M$_\odot$ for MILES compared to 300M$_\odot$ for BPASS). We also note the discussion in Eldridge et al. (2017) regarding the difficulty in reproducing some aspects of old stellar populations using the BPASS models, since they were primarily designed to study populations at less than 1Gyr. We therefore point the interested reader to the papers describing each SSP library for further details; Vazdekis et al. (2015) and Eldridge et al. (2017).

Having said that, the overall trends which we are interested in remain the same for the two sets of measurements. In each case, we see that there is an offset in metallicity between star-forming and passive galaxies at fixed mass, and in both cases we see a tighter correlation between [Z/H] and Φ than between [Z/H] and mass. We therefore find that our conclusions regarding [Z/H], $\log_{10}(M_*/M_\odot)$ and Φ are unchanged regardless whether we use the MILES or BPASS stellar population models.

APPENDIX C: A COMPARISON BETWEEN $[Z/H]_0$ AND $[Z/H]_{R_E}$

A comparison between our results using the central metallicity and the metallicity measured from the $1\ r_e$ spectrum of each galaxy is shown in Figure C1. This choice makes only a marginal difference to the [Z/H] values for each galaxy, leaving our conclusions unchanged. On average, the central metallicity is 0.04 dex larger than the metallicity from within $1\ r_e$. The standard deviation of the difference is 0.15 dex, and a histogram is shown in the inset panel of Figure C1.

APPENDIX D: VELOCITY DISPERSION OR Φ?

Figure D1 shows the relationship between the logarithm of the central velocity dispersion in each galaxy and its value of $\Phi = \log_{10}\left(\frac{M_*}{M_\odot}\right) - \log_{10}\left(\frac{r_e}{kpc}\right)$. The linear relationship is evident above the SAMI instrumental resolution of $\approx 70\ kms^{-1}$. As discussed in Section 6, we use Φ in this work to allow us to include galaxies in this work with $\Phi < 9.5$, without the issue of measuring σ close to the instrumental resolution.

APPENDIX E: A COMPARISON BETWEEN OUR STRAIGHT LINE MODELS

We now present a comparison between the results of the simple straight line fit described in Section 4.1 and the more complicated hierarchical model account for censored data described in Section 4.2.

Figure E1 shows the central metallicity value for each galaxy derived from the hierarchical model accounting for censored data plotted against the value derived from the simple straight line fit. We find a very good agreement between the two, with their difference having mean 0.006 dex and standard deviation 0.05 dex.

This paper has been typeset from a TEX/LATEX file prepared by the author.

a	m_1	m_2	m_3	z_b	τ
-0.09 ± 0.03	-0.50 ± 0.02	-0.03 ± 0.01	-0.82 ± 0.01	-0.53 ± 0.02	0.24 ± 0.01

Table A1. Best fitting parameters of the broken line model used to characterise the uncertainties described in Equation A1.
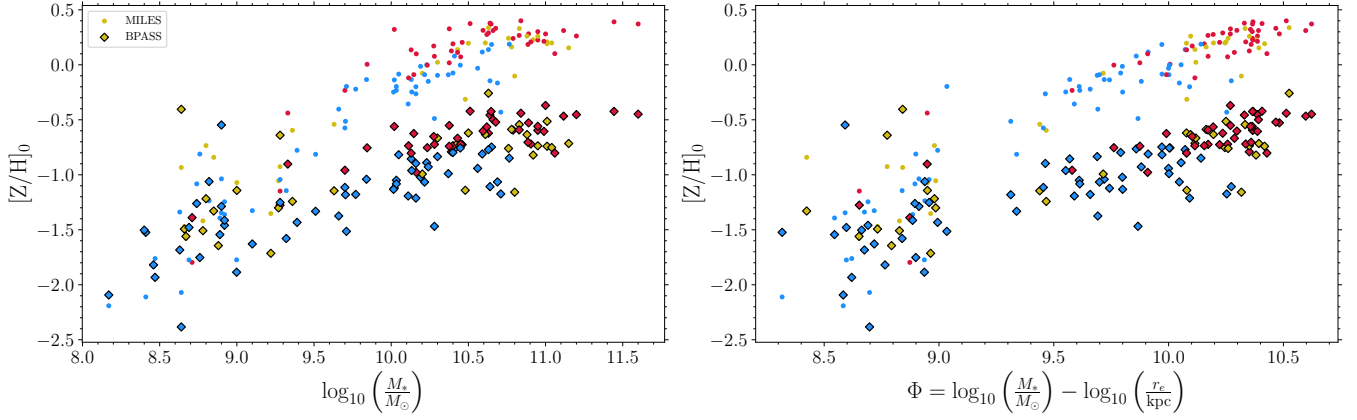

Figure B1. A comparison of the mass-metallicity and Φ-metallicity relations for 130 galaxies in our sample using the MILES models (circles) and BPASS models (diamonds). The colour of each point denotes whether the galaxy is star-forming (blue), passive (red) or "green-valley"/intermediate (yellow), as defined in Section 3. We see that although the BPASS measurements are offset to lower metallicities, especially for galaxies with high values of mass or Φ, the same overall trends remain in both cases.
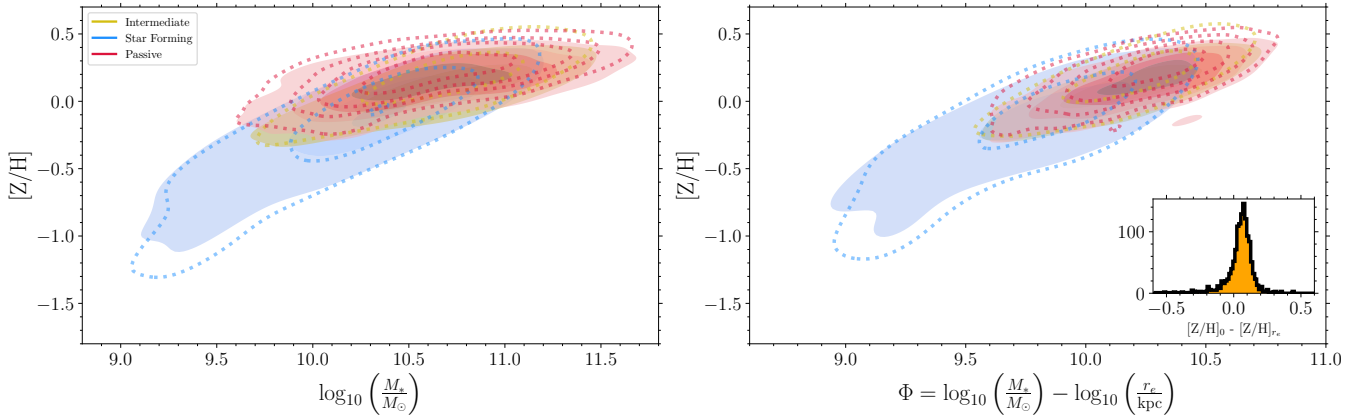

Figure C1. A comparison of the mass-metallicity and Φ-metallicity relations using the central metallicity of each galaxy from the model described in Section 4.2 ($[Z/H]_0$); and the metallicity derived from the 1 r_e spectrum of each galaxy ($[Z/H]_{r_e}$). Shaded density plots correspond to the metallicities from 1 r_e and dotted contour lines show central metallicities. The colours denote the locations of star-forming (blue); passive (red); or intermediate (yellow) galaxies. The inset panel to the right shows the distribution of $[Z/H]_0 - [Z/H]_{r_e}$, which has a mean of 0.04 and a standard deviation of 0.15.
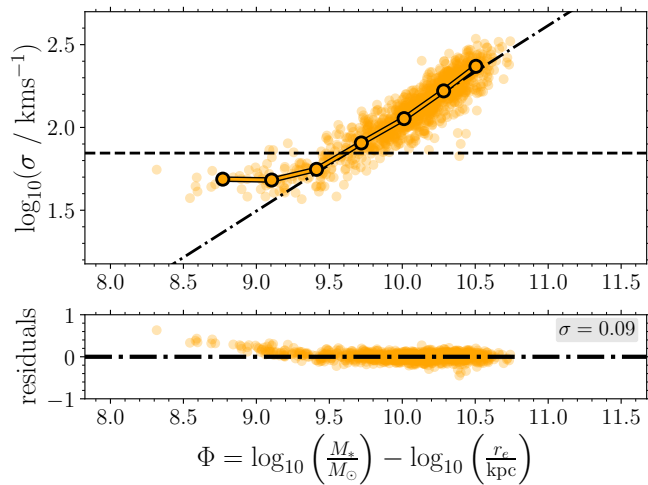
Figure D1. The logarithm of the velocity dispersion of the central Voronoi bin (σ_0) for each galaxy against the galaxy's value of $\Phi = \log_{10}\left(\frac{M_*}{M_\odot}\right) - \log_{10}\left(\frac{r_e}{\mathrm{kpc}}\right)$. The expected linear relationship is clear for galaxies with σ_0 above the SAMI blue-arm instrumental resolution of ≈ 70 kms^{-1} (shown by the dashed line).
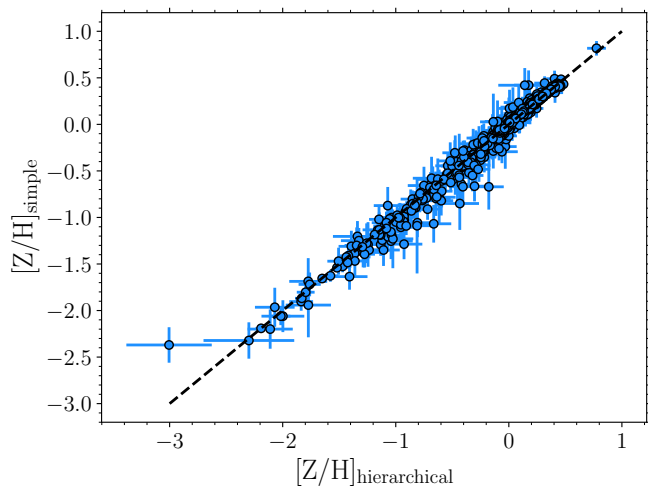

Figure E1. A comparison of the central metallicity value (the straight line intercept) for each galaxy derived from the hierarchical model accounting for censored data (on the *x* axis) and the simple straight line fit (*y* axis). We see a very good agreement between the two. The difference between the two has mean 0.006 dex and standard deviation 0.05 dex.